Journal of
Mechanics of
Materials and Structures

DYNAMICS OF FRP STRENGTHENED UNIDIRECTIONAL MASONRY WALLS I: A MULTILAYERED FINITE ELEMENT

Oded Rabinovitch and Hazem Madah

Volume 7, No. 1 January 2012

mathematical sciences publishers

JOURNAL OF MECHANICS OF MATERIALS AND STRUCTURES
Vol. 7, No. 1, 2012

msp

DYNAMICS OF FRP STRENGTHENED UNIDIRECTIONAL MASONRY WALLS I: A MULTILAYERED FINITE ELEMENT

ODED RABINOVITCH AND HAZEM MADAH

The dynamic response of unidirectional FRP strengthened masonry walls is investigated. The examined walls are strengthened using externally bonded composite materials. In this part of the paper, a nonlinear multilayered finite element for the nonlinear dynamic analysis of the unidirectional strengthened wall is developed. The formulation reduces the general 2D problem to a 1D form using high order kinematic assumptions that are based on the static deformation fields in the various components. The model aims to face the challenges associated with the combination of length scales, differences in elastic properties, irregular points, cracking, crushing, and inelastic behavior of the masonry substrate. The geometrical nonlinearity, the layered configuration, and the variation of the stresses through the depth the adhesive layers are also addressed. A numerical study that examines the capabilities of the model and its convergence with refinement of the spatial and temporal meshes is presented. Emphasis is placed on the global nonlinear dynamic response, the local effects near the joints, the interfacial stresses, and their temporal variation under dynamic loads.

1. Introduction

The strengthening of existing masonry structures by means of externally bonded layers of composite materials is recognized as an advantageous solution for structural upgrade [Albert et al. 2001; Hamilton and Dolan 2001; Griffith et al. 2004; Gilstrap and Dolan 1998]. The demands for upgrade and strengthening mainly stem from the limited (if any) ability of the masonry construction to carry tensile stresses and the resulting vulnerability to dynamic out-of-plane loads. The externally bonded composite layer overcomes this obstacle and provides the existing wall with a strong, stiff, lightweight, and durable tensile resisting layer and thus with a supplemental load resisting mechanism.

The effective design, analysis, and use of masonry walls strengthened with composite material require adequate analytical and computational tools. While finite element analysis (FEA) is the leading computational tool of modern structural engineering, its application to the dynamic analysis of the FRP strengthened masonry wall is involved with significant difficulties. In fact, the entire family of FRP strengthened structural members is a class of structures that their classical 2D or 3D elasticity based FEA is very complicated, computational effort demanding, and, in some cases, subjected to divergence. The problematic nature stems from five major features of the unique structure:

(1) The layered configuration and the assembly of layers of significantly different thickness scale. As a

This research was supported by The Israel Science Foundation, Grant No. 772/06.

Keywords: masonry wall, composite material, nonlinear analysis, dynamic analysis, finite element, nonlinear dynamics, strengthening.

rule, the thickness of the adhesive and the composite layers ranges between parts of a millimeter to few millimeters whereas the thickness of the masonry wall is in the range of hundreds of millimeters.

(2) The different length scales in the masonry construction itself. The masonry construction is an assembly of blocks and mortar joints. The length scale of the blocks (hundreds of millimeters) is much larger than the one of the joints (few millimeters).

(3) The assembly of materials with significantly different elastic properties. In most cases, the elastic modulus of the composite material is two to three orders of magnitude larger than the one of the adhesive layer and about ten times larger than the elastic moduli of the masonry wall.

(4) The presence of structural irregularities in the form of edges of the bonded reinforcement, debonded regions, masonry joints, cracks, etc.

(5) The nonlinearities involved with the structural response. The brittleness of masonry construction, the contact effects at the joints, the nonlinear response of the mortar material under compression, and its inelastic response under cyclic loading introduces material nonlinearities [Hamed and Rabinovitch 2007b; 2008]. Wrinkling and local buckling when the thin FRP strips are subjected to compressive stresses (a scenario that may be inevitable under dynamic loads) and global instability or snap-through of the entire wall [Rabinovitch 2004; Hamed and Rabinovitch 2007a] stem from geometrical nonlinearity. The potential evolution of debonding and interlaminar cracking is involved with interfacial nonlinearities [Rabinovitch 2010].

The combination above yields structural phenomena with length scales that range from the global dimensions of the wall to the thickness of the thinnest layer. The global response can usually be detected using standard techniques. The localized effects associated with stress concentrations near edges and joints, cracking or crushing of the mortar joints, and the transfer of stresses between the masonry wall and the strengthening system are the ones that make the analysis complicated and challenging. The interaction with the dynamic response of the wall and the various nonlinearities make the quantification of the structural response of the dynamically loaded masonry wall even more challenging.

The shortcomings of standard finite element analysis (FEA) of FRP strengthened elements in general, and FRP strengthened masonry walls as a particular case, are reflected by many works that applied FE to the analysis of the strengthened wall. For example, Pan and Leung [2008] studied the effect of tapering of the FRP strip on the debonding process and assessed the edge stresses using two types of FEA. For the elastic case, 8-node quadratic elements with characteristic size of about 1/5 the thickness of the adhesive layer were used. For the nonlinear case, additional nonlinear link elements that account for the degradation of the interfacial shear resistance were added. In both cases, the number of elements required for the analysis of a realistic scale structure is huge. A similar problem was encountered in the 3D FEA presented in [Huang and Lyons 2007]. In this case, the problem of mesh refinement to elements smaller than $1 \cdot 10^{-6}$ of the span was tackled using a submodeling technique. In the substructure, the average element size equals the thickness of the FRP strip and the smaller elements are about two orders of magnitude smaller than that. The finite element model presented in [Li et al. 2009] focused on the interfacial stresses and used elements that are of the same order as the thickness of the adhesive layer. The results of the FEA reveal that in certain cases, the numerical analysis fails to satisfy the zero shear condition at the plate end; see also [Gao et al. 2006; Teng et al. 2002; Rabinovitch and Frostig 2000].

Another aspect, discussed in the last two of these references and in [Hamed and Rabinovitch 2007a], is the divergence of the peak stresses at the critical point; its impact is observed in the FEA results outlined in [Yang et al. 2004]. Due to singularities near irregular points, the critical peak stresses tend to diverge with the refinement of the mesh. This trend shades on the reliability of such analyses and on their applicability to practical design.

The above studies mainly focused on FRP strengthened concrete beams. In general, the dynamic FEA of FRP strengthened walls is even more complicated. The additional levels of complexity are attributed to the effect of cracking, crashing, and geometrical irregularity at the mortar joints and to the unique boundary conditions. Under dynamic loads, the combination of the two phenomena yield a time dependent arching effect, rocking, and coupling between in-plane and out-of-plane responses.

A state of the art FE treatment of the dynamic response of unidirectional externally strengthened masonry members is reported in [Davidson et al. 2005]. This study focuses on masonry walls made of hollow concrete masonry units under blast loads. The walls are strengthened with polymeric layers. The nonlinear FEA focuses on a one-way response and uses a highly refined mesh with as much as 100,000 elements. The analysis accounts for the development of arching effects [Dafnis et al. 2002], the masonry-polymer interfacial response, the high strain rate, and the separation at mortar joints. On the other hand, the large number of elements required for the nonlinear dynamic analysis highlights one of the drawbacks of the conventional FE approach. The same drawbacks also dictate the refined mesh required for the hygrothermal analysis of FRP patched masonry walls described in [Khoshbakht et al. 2009].

The above survey highlights some of the inherent drawbacks of conventional FEA of FRP strengthened elements in general and FRP strengthened masonry walls in particular. In light of these obstacles, Lam et al. [2003] raised concerns about the viability of this type of modeling and pointed in favor of macromodels that simulate the global load-deflection response obtained from experiments. On the other hand, in the case of the strengthened masonry wall, such geometrical homogenization may overlook critical aspects like of the stress concentrations near irregular points.

Analytical models for the static and dynamic nonlinear analysis of FRP masonry walls (see, e.g., [Hamed and Rabinovitch 2007a; 2007b; 2008]) can overcome some of the above critical obstacles. The analytical approach can also handle the combination of global and localized physical effects under a unified analytical platform. The localized stress concentrations near the edges of the FRP system, near the cracked mortar joints, near debonded regions that develop in the vicinity of the cracked joints, and in regions that are wrinkled due to geometrical nonlinearity are taken into account through consideration of the high order stress and deformation fields in the compliant adhesive layers. On the other hand, these models are still limited in terms of the ability of expansion to more demanding problems like bidirectional nonlinear dynamic response and in terms of implementation in more general computational environments for structural analysis.

Specially tailored finite elements for the analysis of layered structures such as sandwich beams or masonry arches strengthened with FRP strips were developed by Buller [Buller 2005] and Elmalich and Rabinovitch [Elmalich and Rabinovitch 2009; Elmalich and Rabinovitch 2010], respectively. However, these models are limited to the linear elastic and static case [Buller 2005], the quasinonlinear, elastic, and static case [Elmalich and Rabinovitch 2009], or the physically nonlinear but static case [Elmalich and

Rabinovitch 2010]. As such, these models cannot address the unique features of the nonlinear, inelastic, and dynamic response of the strengthened masonry wall studied here.

The objective of this part of the paper is to develop a special finite element approach for the nonlinear dynamic analysis of unidirectional FRP strengthened masonry walls. The paper aims to combine the advantages of the analytical models presented in [Hamed and Rabinovitch 2007a; 2007b; 2008] with those of the finite element method and to derive a special finite element for the nonlinear dynamic analysis of the wall. The unique nonlinear dynamic finite element formulation developed here aims to face the challenges stemming from the combined length scales, the different elastic scales, the existence of irregular points, the material nonlinearity of the mortar joints, the layered configuration of the strengthened wall, and some aspects of the geometrical nonlinearity.

Article organization. The modeling assumptions, which follow the analytical models described in the three articles just cited, and the mathematical formulation are presented next. They are followed by a convergence study that examines the capabilities of the finite element model. An experimental study on full scale FRP strengthened wall and comparison of the numerical results with results of the experiments are presented and discussed in the second part of this paper [Rabinovitch and Madah 2012].

2. Finite element model

2.1. ***Modeling and assumptions.*** The strengthened wall, the notation, and the sign conventions appear in Figure 1. The modeling assumptions follow the main analytical concepts described in [Hamed and

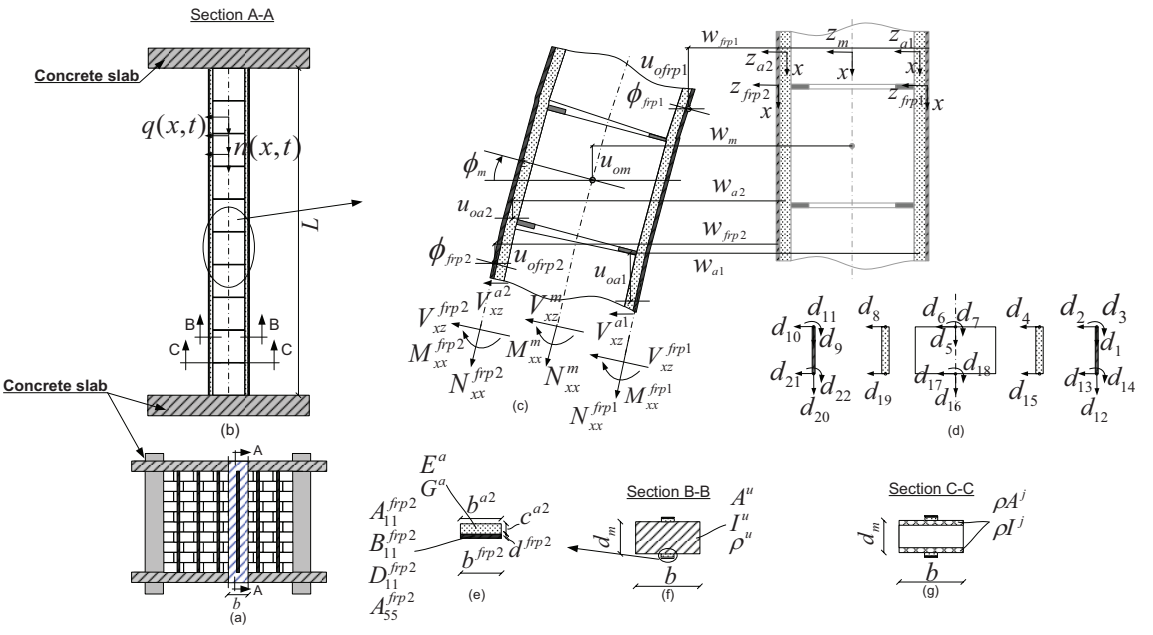

Figure 1. Notation and sign convention: (a) A unidirectional strengthened wall and a characteristic strip. (b) cross section and distributed loads; (c) deformations and stress resultants; (d) degrees of freedom; (e)–(g) cross sections.

Rabinovitch 2007a; 2007b; 2008] and the phenomenological aspects of the wall's response. For simplicity, the formulation focuses on a masonry wall strengthened with vertical FRP strips or with FRP sheets that are extended to the beams or slabs at the top and bottom (Figure 1a). This configuration, and the pattern of bed joints yield vertical flexural "strips" that are stiffer and stronger than the lateral ones and therefore transfer loads more effectively towards the upper and lower supporting element. Under these conditions, as well as in cases where the boundary conditions allow transfer of loads to the upper and the lower supporting elements but not to the lateral ones (if any), it is assumed that the out-of-plane dynamic loads yield a unidirectional flexural action in the height direction. Therefore, it is assumed that the stress and displacement fields are uniform through the width of each component. With these assumptions in mind, the analysis focuses on a characteristic structural strip. In the case of FRP strips, the width of the characteristic strip equals the spacing between two adjacent FRP strips. In the case of FRP sheets, a unit wide characteristic strip is examined.

The characteristics of the strengthened masonry wall require the use of a refined modeling approach that can capture the global behavior but also the localized behavior of each component. In particular, the layered configuration, the differences in material properties, the presence of structural irregularities such as edges, debonded regions, masonry joints, and cracks, the physical nonlinearities of the brittle masonry construction, and the geometrical nonlinearities due to wrinkling, local buckling or global instability motivate a refined and detailed modeling approach. In light of that, the modeling approach adopted in this paper aims to be able to capture the above phenomenological aspects of the FRP strengthened wall. To achieve this, it considers the strengthened wall as a structural element that is composed of five layers. The formulation of each layer is presented using its own coordinate system (Figure 1) and the layers are joined together through the conditions of compatibility of deformations.

Out of the five, the two outer layers are the FRP strips or sheets. These layers, indicated by subscript or superscript "$frp1$" and "$frp2$", are modeled using first-order shear deformation theory (Timoshenko beam; see [Timoshenko and Gere 1961; Reddy 1999]) with an intermediate class of deformations (large deflections, moderate rotations, small strain). The FRP strips are assumed linear elastic and their constitutive behavior is governed by classical lamination theory (see [Vinson and Sierakowski 1986]).

The middle layer is the masonry wall. This layer is comprised of an assembly of masonry units (designated with "mu") and masonry joints (designated with "mj"). Both components are modeled using first order Timoshenko beam theory with large deflections but moderate rotations and small strains. The distinction between the masonry units and the mortar joints comes into effect through their constitutive model. The masonry units are assumed linear and elastic. The mortar material is subjected to cracking, nonlinear behavior under compression, and inelastic behavior under loading-unloading cycles. In that sense, it is assumed that the material nonlinearity that governs the behavior of the masonry construction is concentrated in the mortar joints and introduced through the constitutive model for the mortar material. Since the masonry units and the mortar joints are modeled using the same kinematic assumptions (but with different constitutive relations), both components are designated with the subscript / superscript "m". In cases where the formulation makes a distinction between the two, the notation "mu" and "mj" is used.

The FRP layers are attached to the masonry walls using adhesive layers. These layers, which are designated with the subscripts/superscripts "$a1$" and "$a2$", are modeled as 2D elastic media. The adhesive layers resist shear and out-of-plane normal stresses. Their in-plane rigidities, which are significantly

lower than those of the adjacent components, are neglected (also [Hamed and Rabinovitch 2007a; 2007b; 2008; Rabinovitch and Frostig 2000]). The modeling of the adhesive layers assumes material linearity and, akin to assumption of small strain applied to the masonry wall and the FRP strip, the strains are assumed small.

The entire structural element is mathematically assembled together by imposing continuity and compatibility conditions. The continuity conditions between the masonry units and the mortar joints require continuity of the in-plane displacement, out-of-plane displacement, and cross-sectional rotation. The conditions at the interfaces of the adhesive layers with the FRP layers and the masonry wall require compatibility of the in-plane and out-of-plane displacements. In that sense, it is assumed that the interfaces can transfer the shear and out-of-plane normal stresses stemming from the compatibility conditions. The effect of interfacial debonding, in which the compatibility conditions are relaxed and the interfacial stresses vanish, is not directly addressed here. Alternatively, the physical debonding conditions can be simulated by locally controlling the properties of the materials involved.

The formulation introduces the dissipative effects due to damping through a combination of external (mass proportional) and internal (stiffness proportional) viscous components and the Rayleigh damping model (see, for example, in [Clough and Penzien 1993]). Therefore, the model for the undamped strengthened wall is derived first and then the proportional damping is introduced. Finally, it is assumed that the loads are exerted at the masonry wall only and that the kinematic relations and deformation fields developed for the static case can be applied to the dynamic case as well.

2.2. ***Principle of virtual work.*** The finite element formulation is based on the principle of virtual work. For the undamped structure, the principle of virtual work reads

$$\delta K + \delta' U + \delta W = 0 \tag{1}$$

where δK, $\delta' U$, and δW are the incremental (virtual) works of the inertial forces, stresses, and external loads, respectively. The prime is used to emphasize that U is not necessarily a potential function. The virtual work of the inertial forces is

$$\begin{aligned}
\delta K = -\Bigg[& \int_{V^m} \rho^m \big(\ddot{w}_m(x, z_m, t)\delta w_m(x, z_m, t) + \ddot{u}_m(x, z_m, t)\delta u_m(x, z_m, t)\big)\, dV^m \\
& + \int_{V^{frp1}} \rho^{frp1} \big(\ddot{w}_{frp1}(x, z_{frp1}, t)\delta w_{frp1}(x, z_{frp1}, t) + \ddot{u}_{frp1}(x, z_{frp1}, t)\delta u_{frp1}(x, z_{frp1}, t)\big)\, dV^{frp1} \\
& + \int_{V^{frp2}} \rho^{frp2} \big(\ddot{w}_{frp2}(x, z_{frp2}, t)\delta w_{frp2}(x, z_{frp2}, t) + \ddot{u}_{frp2}(x, z_{frp2}, t)\delta u_{frp2}(x, z_{frp2}, t)\big)\, dV^{frp2} \\
& + \int_{V_{a1}} \rho^{a1} \big(\ddot{w}_{a1}(x, z_{a1}, t)\delta w_{a1}(x, z_{a1}, t) + \ddot{u}_{a1}(x, z_{a1}, t)\delta u_{a1}(x, z_{a1}, t)\big)\, dV^{a1} \\
& + \int_{V^{a2}} \rho^{a2} \big(\ddot{w}_{a2}(x, z_{a2}, t)\delta w_{a2}(x, z_{a2}, t) + \ddot{u}_{a2}(x, z_{a2}, t)\delta u_{a2}(x, z_{a2}, t)\big)\, dV^{a2} \Bigg]
\end{aligned} \tag{2}$$

where ρ^i $(i = m, frp1, frp2, a1, a2)$ is the mass density of the masonry $(i = m)$, the FRP $(i = frp1, frp2)$ and the adhesive $(i = a1, a2)$; $w_i(x, z_i, t)$ and $u_i(x, z_i, t)$ $(i = m, frp1, frp2, a1, a2)$ are the out-of-plane and the in-plane displacements, respectively; V^i is the volume of each component; and $\ddot{}$ represents the second derivative with respect to time, t.

The virtual work of the stresses is

$$\begin{aligned}\delta' U = -\Bigg[& \int_{V^m} \left(\sigma^m_{xx}(x,z_m,t)\delta\epsilon^m_{xx}(x,z_m,t) + \tau^m_{xz}(x,z_m,t)\delta\gamma^m_{xz}(x,z_m,t)\right) dV^m \\ & + \int_{V^{frp1}} \left(\sigma^{frp1}_{xx}(x,z_{frp1},t)\delta\epsilon^{frp1}_{xx}(x,z_{frp1},t) + \tau^{frp1}_{xz}(x,z_{frp1},t)\delta\gamma^{frp1}_{xz}(x,z_{frp1},t)\right) dV^{frp1} \\ & + \int_{V^{frp2}} \left(\sigma^{frp2}_{xx}(x,z_{frp2},t)\delta\epsilon^{frp2}_{xx}(x,z_{frp2},t) + \tau^{frp2}_{xz}(x,z_{frp2},t)\delta\gamma^{frp2}_{xz}(x,z_{frp2},t)\right) dV^{frp2} \\ & + \int_{V^{a1}} \left(\tau^{a1}_{xz}(x,z_{a1},t)\delta\gamma^{a1}_{xz}(x,z_{a1},t) + \sigma^{a1}_{zz}(x,z_{a1},t)\delta\epsilon^{a1}_{zz}(x,z_{a1},t)\right) dV^{a1} \\ & + \int_{V^{a2}} \left(\tau^{a2}_{xz}(x,z_{a2},t)\delta\gamma^{a2}_{xz}(x,z_{a2},t) + \sigma^{a2}_{zz}(x,z_{a2},t)\delta\epsilon^{a2}_{zz}(x,z_{a2},t)\right) dV^{a2}\Bigg] \end{aligned} \tag{3}$$

where $\sigma^i_{xx}(x,z_i,t)$ and $\epsilon^i_{xx}(x,z_i,t)$ are the in-plane normal stresses and strains in the masonry wall ($i=m$) and the FRP ($i=frp1,frp2$); $\tau^i_{xz}(x,z_i,t)$ and $\gamma^i_{xz}(x,z_i,t)$ ($i=m,frp1,frp2,a1,a2$) are the shear stresses and shear angles, respectively; and $\sigma^j_{zz}(x,z_j,t)$ and $\epsilon^j_{zz}(x,z_j,t)$ ($j=a1,a2$) are the out-of-plane normal stresses and strains in the adhesive, respectively. The virtual work of the external loads equals

$$\begin{aligned}\delta W = & \int_{x=0}^{x=H} \left(q_z(x,t)\delta w_m(x,t) + n_x(x,t)\delta u_{0m}(x,t)\right) dx \\ & + \sum_{k=1}^{NC} \int_{x=0}^{x=H} \left(P_k(t)\delta w_m(x_k,t) + N_k(t)\delta u_{0m}(x_k,t) + M_k(t)\delta\phi_m(x_k,t)\right)\delta_D(x-x_k)\,dx \end{aligned} \tag{4}$$

where $q_z(x,t)$ and $n_x(x,t)$ are distributed out-of-plane and in-plane loads, respectively, $P_k(t)$, $N_k(t)$, and $M_k(t)$ are concentrated loads and moments at $x=x_k$, δ_D is Dirac's function, and NC is the number of concentrated loads/moments. (In the physical sense, the concentrated loads stem from knife-edge loads uniformly distributed through the width of the wall).

2.3. *Kinematic and constitutive relations.*

2.3.1. *The masonry wall.* The modeling of the masonry wall applies the same kinematic relations to the masonry units and the mortar joint. The distinction between the two is introduced through their constitutive relations. The kinematic assumptions for the masonry units and the mortar joints use first-order shear deformation theory with an intermediate class of deformations (large deflections, moderate rotations, small strain) as follows:

$$w_m(x,z_m,t) = w_m(x,t), \tag{5}$$

$$u_m(x,z_m,t) = u_{0m}(x,t) - z_m\phi_m(x,t), \tag{6}$$

$$\gamma^m_{xz}(x,z_m,t) = w_{m,x}(x,t) - \phi_m(x,t), \tag{7}$$

$$\epsilon^m_{xx}(x,z_m,t) = u_{0m,x}(x,t) + \tfrac{1}{2}\left(w_{m,x}(x,t)\right)^2 - z_m\phi_{m,x}(x,t), \tag{8}$$

where $u_{0m}(x,t)$ and $\phi_m(x,t)$ are the in-plane displacement at the reference line and the cross-sectional rotation of the masonry unit or the mortar joint, respectively, and subscript , x represents differentiation

with respect to x. The reference line of the masonry wall is located at its middle and z_m is measured from the reference line. The term $\frac{1}{2}(w_{m,x}(x,t))^2$ stems from the general expression for Green's strain tensor in the 1D case and the assumption that the strains are small (and therefore the term $\frac{1}{2}\big(u_{0m,x}(x,t)\big)^2$ is negligible) but the rotations are moderate and therefore considered (see [Fung 1965]). In physical terms, this term reflects the effect of the rotation on the projection of a length segment of the deformed reference axis (see for example, [Brush and Almroth 1975]).

The constitutive model for the masonry wall follows [Rabinovitch and Madah 2011] and introduces the nonlinearity and the inelasticity associated with the masonry construction through the definition of the stress resultants:

$$N^m_{xx} = \int_{A^m} \sigma^m_{xx}\big(\epsilon^m_{xx}(x,z_m,t)\big)\,dA^m = N^m_{xx}(\epsilon^{m0}_{xx}(x,t),\phi_{m,x}(x,t)), \tag{9}$$

$$M^m_{xx} = \int_{A^m} \sigma^m_{xx}(\epsilon^m_{xx}(x,z_m,t))z_m\,dA^m = M^m_{xx}(\epsilon^{m0}_{xx}(x,t),\phi_{m,x}(x,t)), \tag{10}$$

$$V^m_{xz} = \int_{A^m} \tau^m_{xz}(\gamma^m_{xz}(x,z_m,t))\,dA^m = V^m_{xz}(w_{m,x}(x,t),\phi_m(x,t)), \tag{11}$$

where N^m_{xx}, M^m_{xx}, V^m_{xz} are the in-plane, bending, and shear resultants, $\sigma^m_{xx}(\epsilon^m_{xx})$ is the axial stress-strain relation, $\tau^m_{xz}(\gamma^m_{xz})$ is the shear stress-shear strain relation and

$$\epsilon^{m0}_{xx}(x,t) = u_{0m,x}(x,t) + \tfrac{1}{2}\big(w_{m,x}(x,t)\big)^2, \tag{12}$$

where $\epsilon^{m0}_{xx}(x,t)$ is the strain at the reference axis. The stress resultants defined by (9)–(11) also depend on the straining history but opposed to the state variables $u_{0m,x}(x,t)$, $w_m(x,t)$, $\phi_m(x,t)$ and thus $\epsilon^{0m}_{xx}(x,t)$, the strain history is a known function of the spatial coordinates and time.

The model assumes that the material nonlinearity is limited to the mortar joints. The masonry units are therefore assumed linear elastic so that (9)–(11) particularize as follows:

$$N^m_{xx}(x,t) = E^{mu}A^{mu}\epsilon^{m0}_{xx}(x,t), \tag{13}$$

$$M^m_{xx}(x,t) = -E^{mu}I^{mu}\phi_{m,x}(x,t), \tag{14}$$

$$V^m_{xz}(x,t) = \kappa^{mu}G^{mu}A^{mu}\big(w_{m,x}(x,t) - \phi_m(x,t)\big), \tag{15}$$

where E^{mu} and G^{mu} are the elastic and shear moduli of the masonry unit, $E^{mu}A^{mu}$, $E^{mu}I^{mu}$, and $G^{mu}A^{mu}$ are the in-plane, bending, and shear rigidities of the masonry unit cross section, and κ^{mu} is the shear correction factor of the masonry cross section.

In general, the mortar material is brittle and tends to crack under tensile strains. The nonlinear and inelastic compressive behavior for the mortar material depends on the current straining state as well as the loading history, which is designated by the tensor $\boldsymbol{\epsilon}^h$. The response of the mortar material can be approximated by the following expression (also see [Rabinovitch and Madah 2011]):

$$\sigma^m_{xx}(\epsilon^m_{xx},\epsilon^h_{xx}) = \begin{cases} f(\epsilon^m_{xx}) & \text{if } \epsilon^m_{xx} \le \epsilon^h_{xx} \\ f^*(\epsilon^m_{xx},\epsilon^h_{xx}) & \text{if } \epsilon^h_{xx} < \epsilon^m_{xx} \le 0, \\ 0 & \text{if } 0 < \epsilon^m_{xx}, \end{cases} \tag{16}$$

where $f(\epsilon^m_{xx})$ describes the virgin loading path, $f^*(\epsilon^m_{xx}, \epsilon^h_{xx})$ describes the unloading and reloading paths, and ϵ^h_{xx} is the peak negative (compressive) strain at the material point:

$$\epsilon^h_{xx}(x, z, t) = \min_{t^*=0}^{t^*=t}(\epsilon_{xx}(x, z, t^*)) \tag{17}$$

In the present case, the shear stress shear angle relation is approximated by a model that does not take into account the hysteretic or dilatational effects and the coupling with the axial effect excluding the assumption that the cracked mortar material cannot transfer shear (yet, models that are more sophisticated also apply). Under these assumptions, the constitutive law for shear of the mortar material reads:

$$\tau^m_{xz}(\gamma^m_{xz}, \epsilon^m_{xx}) = \begin{cases} s(\gamma^m_{xz}) & \text{if } \epsilon^m_{xx} \le 0, \\ 0 & \text{if } 0 < \epsilon^m_{xx}, \end{cases} \tag{18}$$

where $s(\gamma^m_{xz})$ describes the shear behavior of the compressed mortar.

Introducing (16)–(18) into (9)–(11) defines the cross sectional constitutive relations for the mortar joint. Due to the nonlinearity of the mortar material, they take the form of nonlinear implicit functions of the unknowns and their derivatives.

2.3.2. *The FRP layers.* The FRP layers are also modeled as extensional/flexural members by using first-order shear deformation theory with an intermediate class of deformations. Although the thickness of the FRP layers is generally small (compared with the wall itself) and although their main structural action is in the axial direction, the localized response near irregular points such as edges or mortar joints is involved with localized bending of the layer. In addition, the evolution of compressive forces in the external layer (due to global bending of the strengthened wall or due to the arching effect) may yield localized buckling or wrinkling, which are also involved with flexure of the external layer. Therefore, the flexural action of the FRP layers is also taken into account. Shear deformation theory is adopted for three reasons. First, the shear stiffness of the FRP cross section is usually attributed to the resin matrix whereas the flexural and longitudinal stiffnesses are generally attributed to the fibers. Therefore, the FRP composite may involve shear deformations that are not negligible. Second, the localized region in which flexure and shearing of the FRP laminate take place is usually confined to the close vicinity of the irregular point. In this confined region, the length of the region over the thickness of the FRP strip ratio may be such that shear deformations have an effect. Finally, it is adopted for consistency with the formulation adopted for the masonry wall itself. Since the wall and the FRP layers interact through an adhesive layer, the consistency in the formulation is essential for the soundness of the FE formulation of the adhesive layer. It should also be noted that the modeling of the FRP layers and the modeling of the wall use similar kinematics, however, each layer is modeled independently. The different components are later coupled by means of the conditions of compatible deformations at the interfaces of the adhesive layers. Based on the above, the kinematic relations for the FRP layers read

$$w_{frpi}(x, z_{frpi}, t) = w_{frpi}(x, t), \tag{19}$$

$$u_{frpi}(x, z_{frpi}, t) = u_{0frpi}(x, t) - z_{frpi}\phi_{frpi}(x, t), \tag{20}$$

$$\gamma^{frpi}_{xz}(x, z_{frpi}, t) = w_{frpi,x}(x, t) - \phi_{frpi}(x, t), \tag{21}$$

$$\epsilon^{frpi}_{xx}(x, z_{frpi}, t) = u_{0frpi,x}(x, t) + \tfrac{1}{2}\big(w_{frpi,x}(x, t)\big)^2 - z_{frpi}\phi_{frpi,x}(x, t), \tag{22}$$

where $u_{0frp1}(x,t)$, $u_{0frp2}(x,t)$, $\phi_{frp1}(x,t)$ and $\phi_{frp2}(x,t)$ are the in-plane displacement at the reference line and the cross-sectional rotation of each FRP layer. The reference lines are independently located at the middle of each layer and z_{frpi} are measured from the reference line.

Assuming a linear elastic behavior for the FRP layers, the stress resultants, defined analogously to (9)–(11), can be expressed as follows:

$$N_{xx}^{frpi}(x,t) = A_{11}^{frpi} \cdot \left(u_{0frpi,x}(x,t) + \tfrac{1}{2}\left(w_{frpi,x}(x,t)\right)^2\right) - B_{11}^{frpi} \cdot \phi_{frpi,x}(x,t), \tag{23}$$

$$M_{xx}^{frpi}(x,t) = B_{11}^{frpi} \cdot \left(u_{0frpi,x}(x,t) + \tfrac{1}{2}\left(w_{frpi,x}(x,t)\right)^2\right) - D_{11}^{frpi}(x,t)\phi_{frpi,x}(x,t), \tag{24}$$

$$V_{xz}^{frpi}(x,t) = \kappa^{frpi} A_{55}^{frpi} \cdot \left(w_{frpi,x}(x,t) - \phi_{frpi}(x,t)\right) \tag{25}$$

where A_{11}^{frpi} B_{11}^{frpi}, D_{11}^{frpi} and A_{55}^{frpi} are the extensional, coupling, flexural, and shear rigidities of the inner FRP layer ($i = 1$) or the outer layer ($i = 2$) [Vinson and Sierakowski 1986] multiplied by its width, and κ^{frpi} is the shear correction factor [Reddy 1999]. In the general case where the FRP layer is a composite laminate comprised of orthotropic layers, the rigidities are defined by

$$A_{11}^{frpi} = b \sum_{k=1}^{N_{\text{ply}}} \left(\bar{Q}_{11}^{frpi}\right)_k [h_k - h_{k-1}], \tag{26}$$

$$A_{55}^{frpi} = b \sum_{k=1}^{N_{\text{ply}}} \left(\bar{Q}_{55}^{frpi}\right)_k [h_k - h_{k-1}], \tag{27}$$

$$B_{11}^{frpi} = \frac{b}{2} \sum_{k=1}^{N_{\text{ply}}} \left(\bar{Q}_{11}^{frpi}\right)_k [h_k^2 - h_{k-1}^2], \tag{28}$$

$$D_{11}^{frpi} = \frac{b}{3} \sum_{k=1}^{N_{\text{ply}}} \left(\bar{Q}_{11}^{frpi}\right)_k [h_k^3 - h_{k-1}^3] \tag{29}$$

where $(\bar{Q}_{11}^{frpi})_k$ and $(\bar{Q}_{55}^{frpi})_k$ are the transformed longitudinal and shear stiffnesses of the k-th layer (lamina) within the laminate, N_{ply} is the number of layers, and h_k is the vector distance from the mid-plane of the FRP strip to the lower surface of the k-th layer [Vinson and Sierakowski 1986]. In the general case, B_{11}^{frpi} represents the bending-stretching coupling effect that relates bending moments to mid-surface strains and axial forces to curvatures. When the FRP laminate is symmetric about the mid-surface, this term vanishes [Vinson and Sierakowski 1986].

Note that the above constitutive relations do not take viscoelastic damping into account. Alternatively, the model incorporates them in a global sense based on Rayleigh's model (see, for example, in [Clough and Penzien 1993]). Also, they assume that the rigidities of the FRP layers do not vary in time or along the wall. This assumption well complies with the nature of the type of FRP reinforcement commonly used for strengthening applications.

2.3.3. *The adhesive layers.* The kinematic strain-displacement relations and the constitutive laws for the adhesive layer are based on geometrically linear 2D elasticity and read as follows:

$$\epsilon_{zz}^{ai}(x, z_{ai}, t) = w_{ai,z}(x, z_{ai}, t), \tag{30}$$

$$\gamma_{xz}^{ai}(x, z_{ai}, t) = u_{ai,z}(x, z_{ai}, t) + w_{ai,x}(x, z_{ai}, t), \tag{31}$$

$$\sigma_{zz}^{ai}(x, z_{ai}, t) = E^{ai}\epsilon_{zz}^{ai}(x, z_{ai}, t), \tag{32}$$

$$\tau_{xz}^{ai}(x, z_{ai}, t) = G^{ai}\gamma_{xz}^{ai}(x, z_{ai}, t), \tag{33}$$

where E^{ai} and G^{ai} $(i = 1, 2)$ are the elastic and shear moduli of the adhesive, respectively.

In most classical theories for the dynamics of beams and plates, the static kinematic assumption (i.e., the functional form of the displacement field and the strain-displacement relations) are also applied to the dynamic case. Following this concept, the dynamic displacement field for the adhesive layer is based on the static one (also see [Schwarts-Givli et al. 2007]). The static displacement field of the adhesive layer is derived in [Hamed and Rabinovitch 2007a; 2007b; 2008] by following the concepts outlined in [Rabinovitch and Frostig 2000]. In this field, the out-of-plane displacement takes the form of a parabolic function of the out-of-plane coordinate and the axial displacement takes the form of a cubic function of the out-of-plane coordinate. Under the hypothesis that the longitudinal (axial) stiffness of the adhesive layer is negligible (with respect to the stiffness of the adjacent components) and by means of the kinematic and constitutive relations of (30)–(33), the parabolic and cubic displacement field derived in the references just cited strictly satisfies the static 2D elasticity governing equations of the adhesive medium. However, this solution is expressed in terms of the displacements of the adherents and the shear stress in the adhesive layer. As such, it cannot be implemented in a classical, displacement based, finite element formulation. Alternatively, the functional form of the displacement field derived in the same references; i.e.,the parabolic and cubic out-of-plane and longitudinal displacements, respectively, is adopted here for a displacement based formulation (also see [Buller 2005; Elmalich and Rabinovitch 2009; 2010]). This aims to take advantage of the close form solution of the 2D elasticity equations but yet to handle it through a displacement based form. Following the above approach, the out-of-plane and the in-plane displacements are assumed to take a parabolic and cubic polynomial forms that generally read

$$w_{ai}(x, z_{ai}) = w_{0i}(x) + w_{1i}(x) \cdot \left(\frac{z_{ai}}{c^{ai}}\right) + w_{2i}(x) \cdot \left(\frac{z_{ai}}{c^{ai}}\right)^2, \tag{34}$$

$$u_{ai}(x, z_{ai}) = u_{0i}(x) + u_{1i}(x) \cdot \left(\frac{z_{ai}}{c^{ai}}\right) + u_{2i}(x) \cdot \left(\frac{z_{ai}}{c^{ai}}\right)^2 + u_{3i}(x) \cdot \left(\frac{z_{ai}}{c^{ai}}\right)^3, \tag{35}$$

where $i = 1$ for the inner adhesive layer and $i = 2$ for the outer one; $w_{ji}(x)$ $(j = 0, 1, 2;\ i = 1, 2)$ and $u_{ki}(x)$ $(k = 0, 1, 2, 3;\ i = 1, 2)$ are unknown functions of x only, z_{ai} $(i = 1, 2)$ are the out-of-plane coordinates of the adhesive layer that are measured from the middle of each layer outwards, and c^{a1} and c^{a2} are the thicknesses of the inner and outer adhesive layers, respectively.

The deformation fields of the adhesive layer must satisfy the conditions of compatibility of deformations with the adjacent layers. These conditions read

$$w_{a1}\left(x, z_{a1} = \tfrac{1}{2}c^{a1}\right) = w_m(x), \qquad u_{a1}\left(x, z_{a1} = \tfrac{1}{2}c^{a1}\right) = u_{0m}(x) + \tfrac{1}{2}d^m\phi_m(x), \tag{36}$$

$$w_{a1}\left(x, z_{a1} = -\tfrac{1}{2}c^{a1}\right) = w_{frp1}(x), \qquad u_{a1}\left(x, z_{a1} = -\tfrac{1}{2}c^{a1}\right) = u_{0frp1}(x) - \tfrac{1}{2}d^{frp1})\phi_{frp1}(x), \tag{37}$$

$$w_{a2}\left(x, z_{a2} = \tfrac{1}{2}c^{a2}\right) = w_{frp2}(x), \qquad u_{a2}\left(x, z_{a2} = \tfrac{1}{2}c^{a2}\right) = u_{0frp2}(x) + \tfrac{1}{2}d^{frp2}\phi_{frp2}(x), \tag{38}$$

$$w_{a2}\left(x, z_{a2} = -\tfrac{1}{2}c^{a2}\right) = w_m(x), \qquad u_{a2}\left(x, z_{a2} = -\tfrac{1}{2}c^{a2}\right) = u_{0m}(x) - \tfrac{1}{2}d^m\phi_m(x), \tag{39}$$

where d^m, d^{frp1}, and d^{frp2} are the thicknesses of the masonry wall and the FRP layers, respectively.

Introducing the displacement fields from (34)–(35) into the compatibility conditions (36)–(39) and solving for $w_{11}(x)$, $w_{21}(x)$, $u_{21}(x)$, $u_{31}(x)$, $w_{12}(x)$, $w_{22}(x)$, $u_{22}(x)$, and $u_{32}(x)$ defines 8 out of the 14 unknown functions in terms of the other unknowns. Four of the remaining six unknown functions $[u_{01}(x), u_{11}(x), u_{02}(x), u_{12}(x)]$ are determined by introducing the displacement field back into the static form of the variational principle, i.e., the last two terms in (1), applying the basic lemma of the calculus of variations [Dym and Shames 1973], and solving the algebraic equations that correspond to $\delta u_{01}(x)$, $\delta u_{11}(x)$, $\delta u_{02}(x)$, and $\delta u_{12}(x)$. The last two functions $w_{01}(x)$, $w_{02}(x)$ remain unknown. Thus, the static displacement fields in the adhesive layers take the following form:

$$w_{a1}(x, z_{a1}) = w_{01}(x) + \big(w_m(x) - w_{frp1}(x)\big)\frac{z_{a1}}{c^{a1}} + \big(2w_m(x) - 4w_{01}(x) + 2w_{frp1}(x)\big)\Big(\frac{z_{a1}}{c^{a1}}\Big)^2, \tag{40}$$

$$\begin{aligned} u_{a1}(x, z_{a1}) &= \big(2w_{01,x}(x) - w_{frp1,x}(x) - w_{m,x}(x)\big)\frac{2}{3}\frac{z_{a1}^3}{(c^{a1})^2} + \big(w_{frp1,x}(x) - w_{m,x}(x)\big)\frac{1}{2}\frac{z_{a1}^2}{c^{a1}} \\ &\quad + \big(c^{a1}(w_{m,x}(x) + w_{frp1,x}(x) - 2w_{01,x}(x)) + 6u_{0m}(x) - 6u_{0frp1}(x) + 3d^{frp1}\phi_{frp1}(x) + 3d^m\phi_m(x)\big)\frac{z_{a1}}{6c^{a1}} \\ &\quad + \tfrac{1}{8}(c^{a1}(w_{m,x} - w_{frp1,x}) + 4(u_{0m}(x) + u_{0frp1}(x)) + 2(d^m\phi_m(x) - d^{frp1}\phi_{frp1}(x))) \end{aligned} \tag{41}$$

$$w_{a2}(x, z_{a2}) = w_{01}(x) + \big(w_{frp2}(x) - w_m(x)\big)\frac{z_{a2}}{c^{a2}} + \big(2w_{frp2}(x) - 4w_{01}(x) + 2w_m(x)\big)\Big(\frac{z_{a2}}{c^{a2}}\Big)^2 \tag{42}$$

$$\begin{aligned} u_{a2}(x, z_{a2}) &= \big(2w_{01,x}(x) - w_{0,x}(x) - w_{frp2,x}(x)\big)\frac{2}{3}\frac{z_{a2}^3}{(c^{a2})^2} + \big(w_{m,x}(x) - w_{frp2,x}(x)\big)\frac{1}{2}\frac{z_{a2}^2}{c^{a2}} \\ &\quad + \big(c^{a2}(w_{frp2,x}(x) + w_{m,x}(x) - 2w_{01,x}(x)) + 6u_{0frp2}(x) - 6u_{0m}(x) + 3d^m\phi_m(x) + 3d^{frp2}\phi_{frp2}(x)\big)\frac{z_{a2}}{6c^{a2}} \\ &\quad + \tfrac{1}{8}(c^{a2}(w_{frp2,x}(x) - w_{m,x}(x)) + 4(u_{0frp2}(x) + u_{0m}(x)) + 2(d^{frp2}\phi_{frp2}(x) - d^m\phi_m(x))) \end{aligned} \tag{43}$$

Analogously to the common case where the static displacement field is used for the dynamic analysis, (40)–(43) are applied to the dynamic case, yielding

$$\begin{aligned} &w_{a1}(x, z_{a1}, t) \\ &\quad = w_{01}(x, t) + \big(w_m(x, t) - w_{frp1}(x, t)\big)\frac{z_{a1}}{c^{a1}} + \big(2w_m(x, t) - 4w_{01}(x, t) + 2w_{frp1}(x, t)\big)\Big(\frac{z_{a1}}{c^{a1}}\Big)^2, \end{aligned} \tag{44}$$

$$\begin{aligned} &u_{a1}(x, z_{a1}, t) \\ &\quad = \big(2w_{01,x}(x, t) - w_{frp1,x}(x, t) - w_{m,x}(x, t)\big)\frac{2}{3}\frac{z_{a1}^3}{(c^{a1})^2} + \big(w_{frp1,x}(x, t) - w_{m,x}(x, t)\big)\frac{1}{2}\frac{z_{a1}^2}{c^{a1}} \\ &\qquad + \big(c^{a1}(w_{m,x}(x, t) + w_{frp1,x}(x, t) - 2w_{01,x}(x, t)) \\ &\qquad\quad + 6u_{0m}(x, t) - 6u_{0frp1}(x, t) + 3d^{frp1}\phi_{frp1}(x, t) + 3d^m\phi_m(x, t)\big)\frac{z_{a1}}{6c^{a1}} \\ &\qquad + \tfrac{1}{8}\big(c^{a1}(w_{m,x}(x, t) - w_{frp1,x}(x, t)) + 4(u_{0m}(x, t) + u_{0frp1}(x, t)) + 2(d^m\phi_m(x, t) - d^{frp1}\phi_{frp1}(x, t))\big), \end{aligned} \tag{45}$$

$$\begin{aligned} &w_{a2}(x, z_{a2}, t) \\ &\quad = w_{01}(x, t) + \big(w_{frp2}(x, t) - w_m(x, t)\big)\frac{z_{a2}}{c^{a2}} + \big(2w_{frp2}(x, t) - 4w_{01}(x, t) + 2w_m(x, t)\big)\Big(\frac{z_{a2}}{c^{a2}}\Big)^2 \end{aligned} \tag{46}$$

$$u_{a2}(x, z_{a2}) = \big(2w_{01,x}(x) - w_{01,x}(x) - w_{frp2,x}(x)\big)\frac{2}{3}\frac{z_{a2}^3}{(c^{a2})^2} + \big(w_{m,x}(x) - w_{frp2,x}(x)\big)\frac{1}{2}\frac{z_{a2}^2}{c^{a2}} \tag{47}$$
$$+\big(c^{a2}(w_{frp2,x}(x) + w_{m,x}(x) - 2w_{01,x}(x)) + 6u_{0frp2}(x) - 6u_{0m}(x) + 3d^m\phi_m(x) + 3d^{frp2}\phi_{frp2}(x)\big)\frac{z_{a2}}{6c^{a2}}$$
$$+\tfrac{1}{8}\big(c^{a2}(w_{frp2,x}(x) - w_{m,x}(x)) + 4(u_{0frp2}(x) + u_{0m}(x)) + 2(d^{frp2}\phi_{frp2}(x) - d^m\phi_m(x))\big).$$

The formulation presented in [Hamed and Rabinovitch 2008] uses the displacements and shear stress as unknowns. This leads to the introduction of additional assumptions and neglects of the high order terms in the distributions of velocities and accelerations. Opposed to that, the formulation presented here is based on displacement unknowns only and, therefore, the velocity and acceleration fields are directly determined by the temporal derivatives of (44)–(47). In addition, the use of a displacement formulation allows for a direct implementation in the finite element formulation, which is discussed next.

2.4. ***Finite element approximation.*** The FE approximation of the displacements reads:

$$v_i \approx v_i^h = \sum_{A \in S_{vi}} N_A(x) d_A(t), \tag{48}$$

$$\delta v_i \approx \delta v_i^h = \sum_{A \in S_{vi}} N_A(x) \delta d_A(t), \tag{49}$$

where $d_A(t)$ are generalized unknown displacements, $\delta d_A(t)$ are virtual displacements; $N_A(x)$ are shape function, v_i is the i-th entry of the unknown displacements vector

$$\boldsymbol{v} = [u_{0frp1}, u_{0m}, u_{0frp2}, w_{frp1}, w_m, w_{frp2}, \phi_{frp1}, \phi_m, \phi_{frp2}, w_{01}, w_{02}]^T,$$

and s_{v_i} is the group of shape functions that correspond to the unknown function v_i. Introducing the FE approximation — see (48) and (49) — into the principle of virtual work, Equation (1), and applying the basic lemma of the calculus of variations [Dym and Shames 1973] yields the standard form of equations of motion:

$$\boldsymbol{M}\ddot{\boldsymbol{d}}(t) + \boldsymbol{g}(\boldsymbol{d}(t)) - \boldsymbol{P}(t) = \boldsymbol{0}, \tag{50}$$

where $\boldsymbol{d}(t) = [d_A(t)]$ is the vector of unknown displacements, $\boldsymbol{M} = [M_{AB}]$ is the mass matrix, $\boldsymbol{g}(\boldsymbol{d}(t)) = [g_A(\boldsymbol{d}(t))]$ is a set of nonlinear functions of the unknown functions $\boldsymbol{d}(t)$, and $\boldsymbol{P}(t)$ is a vector of external loads. If $d_A(t)$ is prescribed, the A-th equation in (50) is replaced with

$$d_A(t) - \bar{d}_A(t) = 0, \tag{51}$$

where $\bar{d}_A$ is the prescribed displacement.

The FE form of the initial conditions read

$$\left.\begin{aligned} d_A(0) &= \bar{d}_A(0) \\ \dot{d}_A(0) &= \bar{\dot{d}}_A(0) \end{aligned}\right\} \quad \text{for all } A, \tag{52, 53}$$

where $\bar{d}_A(0)$ and $\bar{\dot{d}}_A(0)$ are prescribed displacements and velocities at $t = 0$.

The present formulation uses the simplest linear ("tent") shape functions for all 11 unknowns:

$$\left.\begin{aligned} N_i &= 1-(x-x_e)/l_e \\ N_j &= (x-x_e)/l_e \end{aligned}\right\} \quad \text{for } x \in [x_e, x_e+l_e], \tag{54}$$

(55)

where x_e is the upper coordinate of the element, l_e is the length of the element; N_i corresponds to the upper (i-th) node,and N_j corresponds to the lower (j-th) node. The element includes 11 degrees of freedom at each node. The elemental DOFs are illustrated in Figure 1d.

The global mass matrix, the tangent matrix, the nonlinear vector, and the load vector are evaluated at the element level and then assembled into the global scale:

$$\boldsymbol{M} = \boldsymbol{A}_e(\boldsymbol{M}_e), \tag{56}$$

$$\boldsymbol{K} = \frac{\partial \boldsymbol{g}(\boldsymbol{d}(t))}{\partial \boldsymbol{d}(t)} = \boldsymbol{A}_e\Big(\frac{\partial \boldsymbol{g}_e(\boldsymbol{d}_e(t))}{\partial \boldsymbol{d}_e(t)}\Big), \tag{57}$$

$$\boldsymbol{g}(\boldsymbol{d}(t)) = A_e\big(\boldsymbol{g}_e(\boldsymbol{d}_e(t))\big), \tag{58}$$

$$\boldsymbol{P}(t) = A_e\big(\boldsymbol{P}_e(t)\big) + \boldsymbol{P}_{\text{node}}(t), \tag{59}$$

where the subscript e designates the element level, $\boldsymbol{A}_e$ is the assembly operator for matrices, A_e is the assembly operator for vectors, and $\boldsymbol{P}_{\text{node}}(t)$ is a vector of concentrated loads at the joints.

The effect of damping is introduced using the simplest Rayleigh model. By means of this approximation, the equation of motion (46) changes to

$$\boldsymbol{M}\cdot\ddot{\boldsymbol{d}}(t) + \boldsymbol{C}\cdot\dot{\boldsymbol{d}}(t) + \boldsymbol{g}(\boldsymbol{d}(t)) - \boldsymbol{P}(t) = \boldsymbol{0}, \tag{60}$$

where $\boldsymbol{C}$ is the proportional damping matrix given by:

$$\boldsymbol{C} = \alpha_0\boldsymbol{M} + \alpha_1 \frac{\partial \boldsymbol{g}}{\partial \boldsymbol{d}}\Big|_{d(t)=\boldsymbol{0}^-}. \tag{61}$$

The proportionality factors α_0 and α_1 of Rayleigh's damping model are assessed by prescribing the damping ratio at two selected modes [Clough and Penzien 1993].

The formulation above yields two types of elements. The first one uses the constitutive relations in the form of (13)–(15) and corresponds to the masonry units. The second element uses the constitutive relations of (9)–(11) and corresponds to the mortar joints. Both types of elements are assembled into the global model.

The nonlinear initial value problem given by (60) and (51) with the initial conditions in (52) and (53) is transformed into a set of successive nonlinear algebraic problems using Newmark's method [1959]. These equations are solved at every time step for $\boldsymbol{d}(t_i)$ using the Newton method. Unlike the formulation presented in [Hamed and Rabinovitch 2008], which used direct iterations with updated secant moduli, the present iterative scheme takes advantage of the quadratic convergence of the Newton method. This advantage simplifies the analysis and improves its convergence characteristics. Furthermore, it simplifies its implementation in a more general finite element based computational environment.

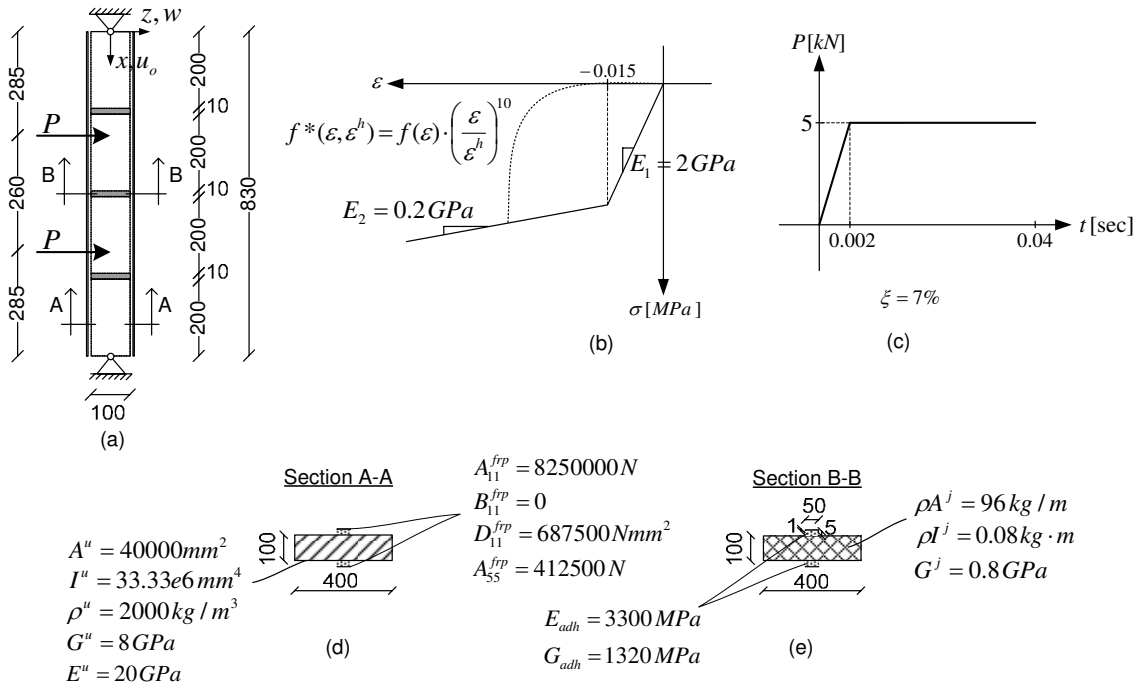

Figure 2. Geometry, loading, and mechanical properties for the convergence study (a) geometry and loading (dimensions are in mm); (b) stress-strain curve for the mortar material (c) dynamic loading scheme (d) cross section and elastic properties of the masonry units and the FRP strips; (e) cross section and elastic properties of the mortar joints and the adhesive layers.

3. Numerical convergence study

In this section, the behavior of a small-scale strengthened wall specimen is examined numerically. The study includes two cases. First, the effect of refinement of the mesh on the numerical analysis of the response to a static load is examined. Then, the effect of the mesh characteristics and the size of the time step on the dynamic response to a step load is examined.

The geometry, loading, supporting, and material properties of the specimen appear in Figure 2. The width of the examined strip equals 400 mm and it is strengthened using two 50 mm wide CFRP strips, one strip on each face. In order to allow several steps of mesh refinement, the study focuses on a relatively small specimen that is comprised of four masonry units and three joints. As in many practical cases, it is assumed that the construction technique does not provide the upper and the lower units with a sufficient rotational constraint yielding simply supported conditions. In the first case, the wall is subjected to two static concentrated loads. The magnitude of each load equals 5 kN. In the second case, the wall is subjected to the same loading scheme but the out-of-plane load is applied dynamically as shown in Figure 2c. In practice, masonry walls are usually subjected to compressive loads, either due to their self weight or due to load transferred by adjacent structural elements such slabs or beams. In order to

take at least some aspects of this effect into account, the examined wall specimens are also subjected to axial precompression load. In both analyses, this load equals 6 kN and it is applied by prescribing the displacement at the top support. It should be noted that the magnitude of the precompression load is relatively high (compared with the dynamic out-of-plane load) yet, the precompressive stains it yields in the mortar joints are relatively small and well within the initial stiffer range of the loading stress-strain curve.

3.1. ***Response to a static load.*** Four finite element meshes are examined. The meshes are titled M1–M4 and their properties appear in Table 1. In meshes M1–M3, the nodes are equally spaced along the specimen. Mesh M4 uses smaller elements for the joint region. The element size ranges form about the thickness of the externally bonded layers to about one tenth of this measure (see Table 1). Since the problem at hand does not have an analytical closed form solution, the convergence of the numerical analysis and the measure of accuracy are defined with respect to the most refined mesh (M4). The run time of the analysis is selected as a measure of the computational efficiency. These measures, normalized with respect to the run time with mesh M1 appear in Table 1 and quantify the increase in computational effort associated with the refinement of the mesh. It appears that mesh M4, which is not involved with a significant increase in number of DOFs, is involved with a significant increase in run. This is attributed to the increased number of nonlinear joint elements.

The out-of-plane deflections and the in plane deflections in the masonry specimen and the FRP strips appear in Figure 3. In that figure, as in the ones that follow, the circular markers designate the nodes of the finite element mesh. The nodes are connected by straight lines. The global scale distribution of the out-of-plane deflections (Figure 3, top) clearly reveals the sharp rotation at the joint. Zoom plots on the compressed FRP strip, the masonry wall, and the tensioned FRP strip appear in the second row of graphs in Figure 3, and reveal the effect of the rotation of the joint on the localized deformations. It is also observed that the peak out-of-plane deformations of the FRP strips are slightly smaller than that of the masonry wall. This effect, which is attributed to the out-of-plane deformability of the adhesive layer, is more pronounced in the tensioned layer where the strip is compressed against the adhesive layer and the masonry wall.

The comparison between the different meshes reveals only minor differences that consistently vanish with refinement. It seems that the results obtained with mesh M1 are slightly too coarse, but the ones obtained with mesh M2 and M3 are satisfactorily close to the results obtained with mesh M4. This implies that in the present case, the extensive computation effort required for mesh M4 is not required.

Mesh	No. of elements through joint	No. of elements through the unit	Total no. of DOFs	Size of smallest element [mm]	Run time (normalized w.r.t. M1)	Line style in Figures 3–7
M1	2	40	1837	5.000	1	– · – · –
M2	4	80	3663	2.500	2.12	– – –
M3	8	160	7315	1.250	5.12	· · · · · ·
M4	24	160	7843	0.416	7.07	——

Table 1. Mesh properties for static analyses.

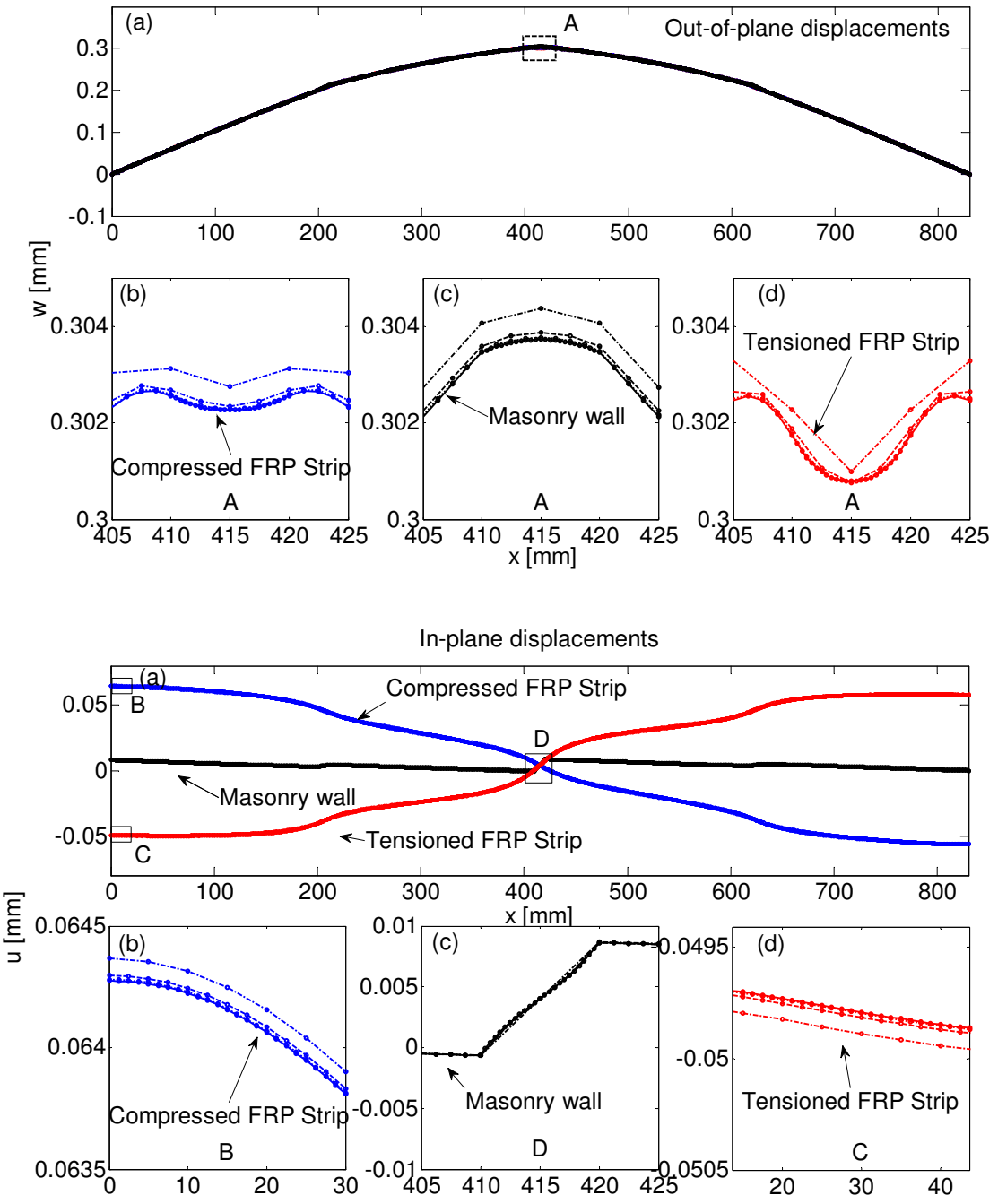

Figure 3. Distributions of out-of-plane (top half) and in-plane (bottom half) deflections along the wall, for different meshes. In each case, part (a) shows the global distributions, and parts (b)–(d) zoom in on a specific zone of (a), showing the deflections of the compressed FRP strip (b), the wall (c), and the tensioned FRP strip (d). Legend: — · — · — Mesh M1; — — — Mesh M2; · · · · · · Mesh M3; —— Mesh M4, ∘ FE nodes.

The axial deformations are studied in the bottom half of Figure 3. Also here, the global scale results as well as the zoom plots reveal the effect of the cracking at the joint and the asymmetry due to the precompression. In terms of convergence, the differences between the various meshes are even smaller than the ones observed in the top half of the figure. Even near the joint — part (c) in bottom row — or near the edges of the strips — parts (b) and (d) on bottom row — the division of the joint to 2 elements (M1) yields a reasonable assessment and the differences between the meshes M2, M3, and M4 are negligible.

The bending moment, axial forces, and shear forces in the FRP strips and in the masonry wall are studied in Figure 4, respectively. The distributions of the bending moments (top half of figure) and the axial forces (bottom half) reveal the transition of the global bending moment resistance mechanism near the joint. Due to cracking of the joint, the flexural stiffness of the wall drops down and a larger portion of the global bending moment is carried in the form a force couple with tension in the outer FRP strip and compression in the wall. As a result, the axial force in the tensioned strip is amplified and the bending moment in the masonry wall is reduced. Note that the axial forces (bottom half of Figure 4) sum up to a level of compression higher than the applied precompression. This is attributed to the arching effect. The cracking of the joints shifts the axis of rotation of the cracked joint form the level of the mid-surface to the level of the crack tip. On the other hand, the axis of rotation at the supports (in the case studied here) remains at the mid-surface level. As a result, the out-of-plane displacement of the wall and the rotation of the relatively stiff masonry blocks push the outer blocks against the supports. Since both supports are longitudinally fixed, this process results in a build-up of a compressive force and an "arch" type of action. In the present case, this effect is much more significant than the influence of the precompression.

The comparison between the different analyses reveals minor differences between meshes M2-M4. The coarse mesh (M1) does not provide sufficiently smooth and accurate results, but the more refined meshes do. Even mesh M2, in which the joint is divided to four elements, provides a reasonable assessment of the distributions of the axial forces and the bending moments. The zoom plots on the middle joint, displayed in parts (b)–(d) of Figure 4, top and bottom, show that the results with the intermediate meshes M2 and M3 almost coincide with the analysis with mesh M4. Figure 5, on the other hand, indicates that the distributions of the shear forces are more sensitive to the size of the element. The zoom plot on the upper joint reveals differences that are not very prominent. On the other hand, the distributions of the shear forces in the FRP strips near the edges are slightly different. In this region, the analysis with mesh M1 yields a "zig-zag" pattern around the results obtained with the refined meshes. This "zig-zag" effect becomes less significant with mesh M2 and it vanishes with mesh M3.

Figure 5 also reveals that the distributions of the shear forces exhibit rapid and significant variations near the cracked joints. This is an outcome of the development of shear stress concentrations in the adhesive layers, which can be observed in Figure 6. The total (or "global") shear force, which is the sum of the shear forces in all structural components, takes into account the sum of the shear forces carried by the wall and the FRP strips as well as the shear forces that develop in the adhesive layers. In the present formulation, which is derived in the framework of the variational calculus, all shear forces are defined as the variational counterparts of the corresponding out-of-plane displacements. Near the joints, the shear forces that develop in the adhesive layer are significantly amplified (as a result of the change in the bending resistance mechanism form the block region to the joint region). Consequently, the shear resultants in the adhesive layer (defined as the variational counterparts of w_{01} and w_{02}) become nonnegligible. This component provides the "missing" contribution to the global shear equilibrium.

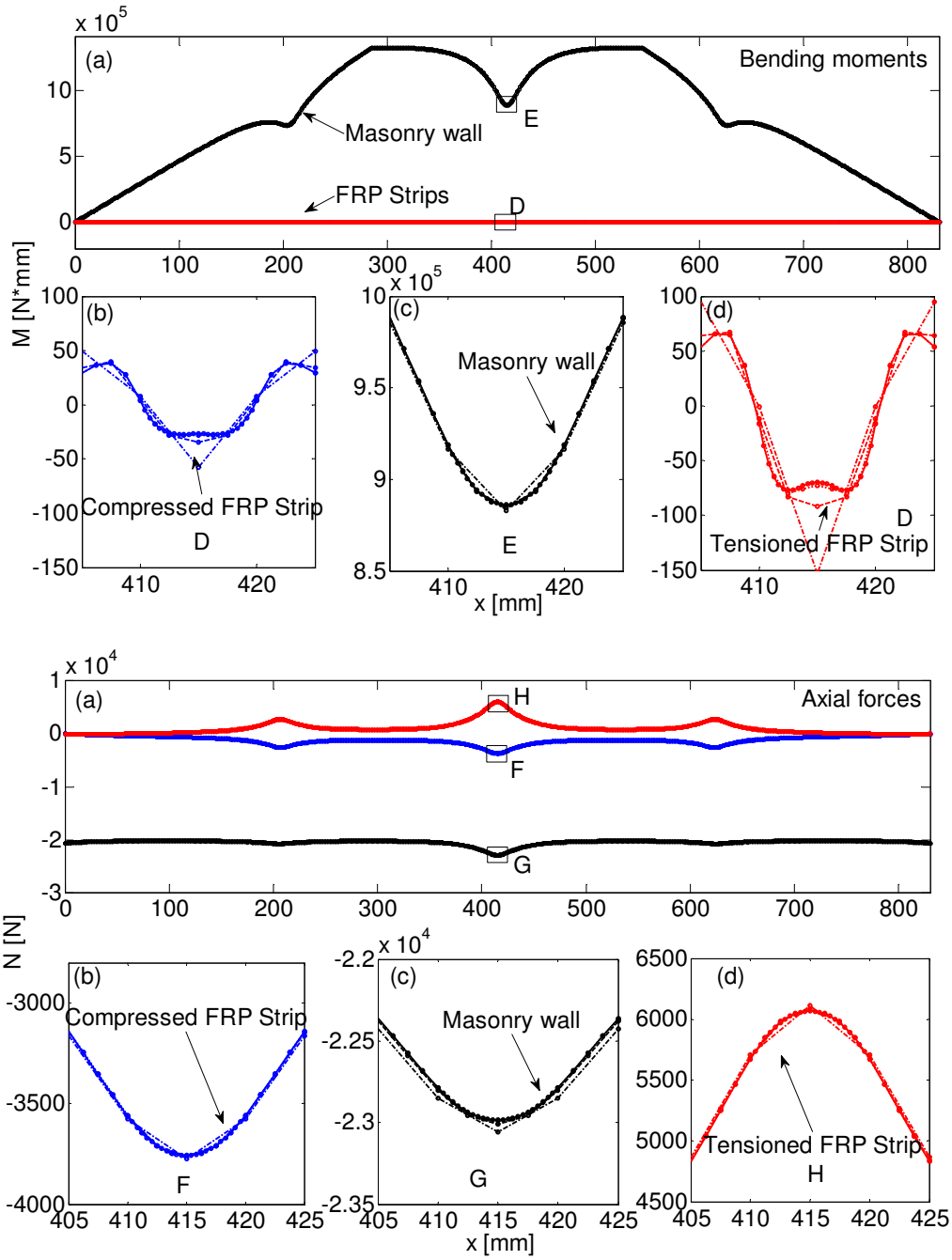

Figure 4. Distributions of bending moments (top) and axial forces (bottom) along the wall. In each case, part (a) shows the global distributions, and parts (b)–(d) zoom in on a specific zone of (a), showing the bending moments or axial forces in the compressed FRP strip (b), the wall (c), and the tensioned FRP strip (d). Legend: – · – · – Mesh M1; – – – Mesh M2; · · · · · · Mesh M3; —— Mesh M4, ∘ FE nodes.

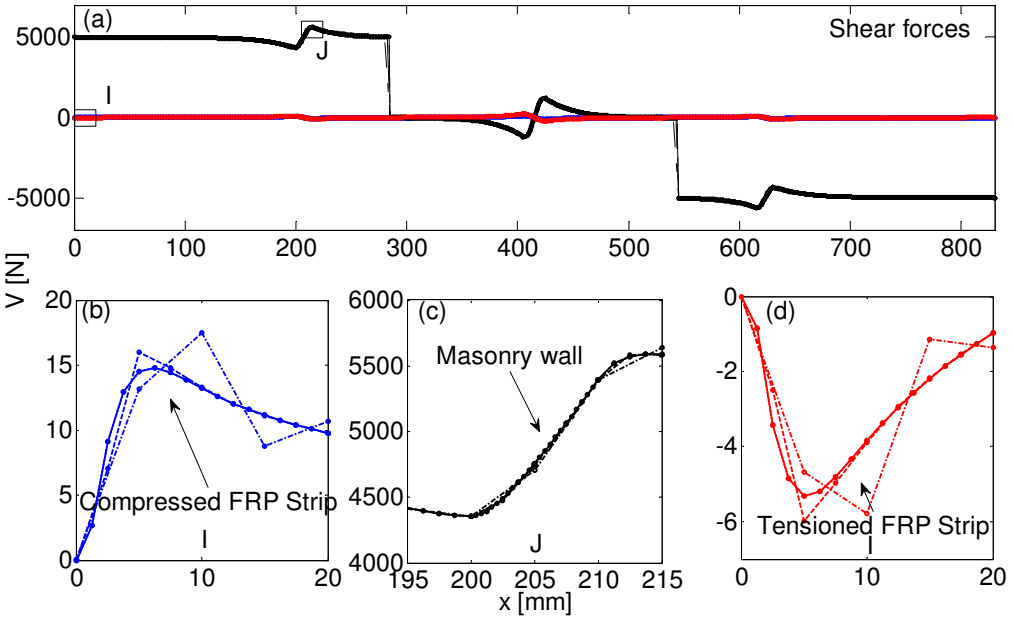

Figure 5. Distributions of shear forces along the wall: (a) global distributions; (b) shear forces in the compressed FRP strip at zone "I"; (c) shear forces in the wall at zone "J"; (d) shear forces in the tensioned FRP strip at zone "I". Legend: $-\cdot-\cdot-$ Mesh M1; $---$ Mesh M2; $\cdots\cdots$ Mesh M3; —— Mesh M4, $\circ$ FE nodes.

Thus, the sum of the shear forces in the two FRP layer, the two adhesive layers, and the wall itself strictly corresponds to the value deduced by global equilibrium. Nevertheless, the localized evolution of shear concentrations in the adhesive interfaces near the joint is a critical aspect of the response of the strengthened wall specimen. This aspect, as well as the evolution of out-of-plane normal stresses and their anticipated impact in terms of the numerical sensitivity of the FE model, are studied next.

The distributions of the shear stresses that appear in Figure 6 reveal the significant stress concentrations near the joints. The global scale distributions indicate that the stresses observed in the adhesive layer that bonds the tensioned FRP strip are higher than those observed in the adhesive layer that bonds the compressed strip. This pattern is in agreement with the distribution of the axial forces that develop in the FRP strips (Figure 4, bottom). The zoom plots on the stresses near the edge (Figures 6b and 6c) and near the middle joint (Figures 6d and 6e) reveal that also here the analysis with the coarse mesh (M1) yields a "zig-zag" pattern. The refined meshes M2 and M3 reveal a more smooth behavior and converge towards the finer mesh M4.

Figures 6b and 6c also show that with all meshes, the zero shear boundary condition at $x = 0$ is satisfied. In that sense, the present FE model overcomes one of the drawbacks observed in standard (2D elasticity based) FE analysis of FRP strengthened elements. The distributions of the out-of-plane normal stresses at the interfaces of the adhesive layers are studied in Figure 7. The global scale results shown in the graphs (a), top and bottom, quantify the stress concentrations that develop near the cracked joints and near the edges of the FRP strip. They also reveal that the FE model captures the variation of the

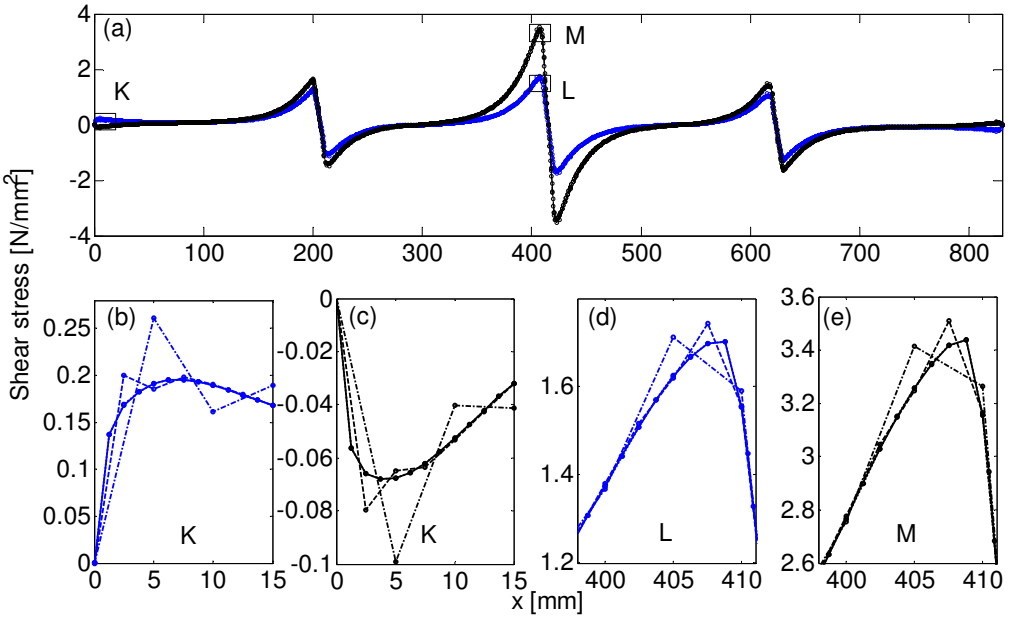

Figure 6. Distributions of shear stresses in the adhesive layers: (a) global distributions; (b) near the edge of the compressed FRP strip (zone "K"); (c) near the edge of the tensioned FRP strip (zone "K"); (d) near the middle of the compressed FRP strip (zone "L"); (e) near the middle of the tensioned FRP strip (zone "M"). Legend: $-\cdot-\cdot-$ Mesh M1; $---$ Mesh M2; $\cdots\cdots$ Mesh M3; —— Mesh M4, $\circ$ FE nodes.

stresses though the depth of the adhesive layer. The comparison between the graphs (a) in the top and bottom parts of Figure 7 implies that in this case, the stress concentrations near the tensioned strip (top) are significantly higher than the ones near the compressed strip (bottom).

The zoom plots that appear in Figure 7 reveal that the analysis with the coarse mesh M1 is strongly affected by the "zig-zag" behavior. This analysis does not provide a satisfactory description of the response. Near the middle joint, for example, the analysis with mesh M1 overestimates the compressive stresses at the adhesive-FRP interface and does not capture the transition from tension to compression at the adhesive-masonry interface; see graphs (d) and (e), respectively, in the top part of Figure 7. The analyses with the refined meshes yield a better description of the interfacial stresses. The differences between meshes M3 and M4 are rather negligible and even mesh M2 provides a reasonable description of the interfacial stresses.

The above results demonstrate that the FE model can effectively handle the localized effects, in spite of the order of magnitude deviation of characteristic length scales. It is also observed that the peak values observed at the edges of the adhesive layer are not sensitive to the mesh characteristics and the values obtained by the four analyses are very close. This demonstrates that the present formulation is not subjected to divergence near the irregular point. In that sense, it overcomes another drawback of the standard FE analysis of FRP strengthened flexural members.

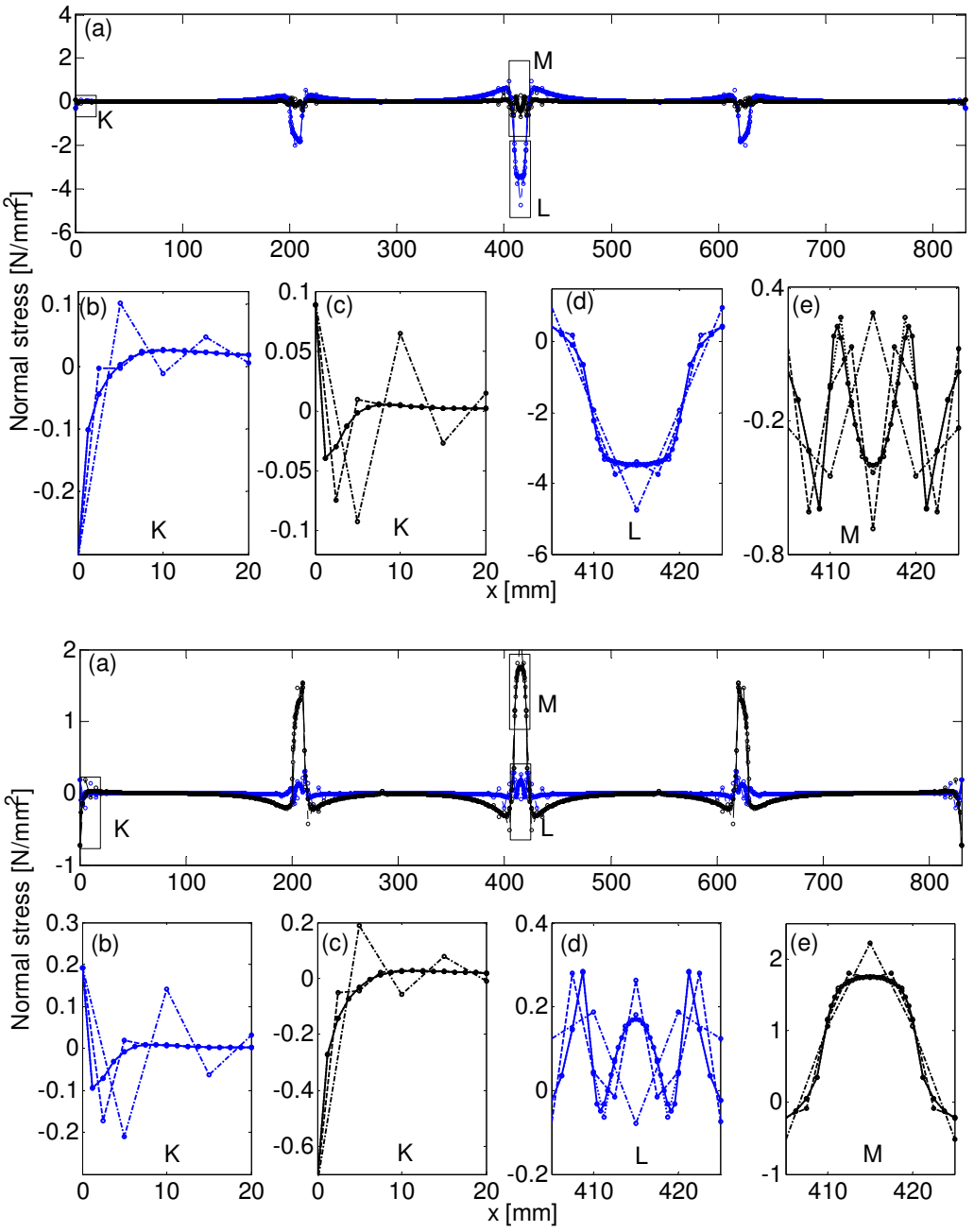

Figure 7. Distributions of normal out-of-plane stresses in the adhesive layers bonding the tensioned (top) and compressed (bottom) FRP strip. (a) global distributions; (b) adhesive-FRP interface near the edge (zone "K"); (c) adhesive-masonry interface near the edge (zone "K"); (d) adhesive-FRP interface near the middle joint (zone "L"); (e) adhesive-masonry interface near the middle joint (zone "N"). Legend: $-\cdot-\cdot-$ Mesh M1; $---$ Mesh M2; $\cdots\cdots$ Mesh M3; —— Mesh M4, $\circ$ FE nodes.

Mesh	No. of elements through joint	No. of elements through the unit	Total No. of DOFs	Time step [mili-sec]	Run-time (normalized w.r.t. M2T1)	Line style in Figures 8–11
M2T1	4	80	3663	0.25	1.00	– · – · –
M3T1	8	160	7315	0.25	2.64	– – –
M2T2	4	80	3663	0.125	1.84	· · · · · ·
M3T2	8	160	7315	0.125	4.51	——

Table 2. Mesh properties for dynamic analyses.

3.2. ***Response to dynamic load.*** This section examines the dynamic response of the strengthened specimen to the loading described in Figure 2c. The two intermediate meshes, M2 and M3, and two time steps, 0.25 ms and 0.125 ms, are examined. The larger time step is about 1/25 the period of the first vibration mode of the specimen. The analyses with the larger time step are designated with T1 and the analyses with the smaller time step are designated with T2. Therefore, the four examined combination are designated M2T1, M2T2, M3T1, and M3T2. The properties of the various meshes are summarized in Table 2. The damping coefficients are selected to yield 7% damping ratio in the first two elastic modes. In the figures discussed in the following paragraphs, the circular marks designate the time steps.

The temporal variation of the out-of-plane deflections at mid-height is studied in Figure 8. The results reveal the typical response to a step load and mainly the transient response that is damped towards a

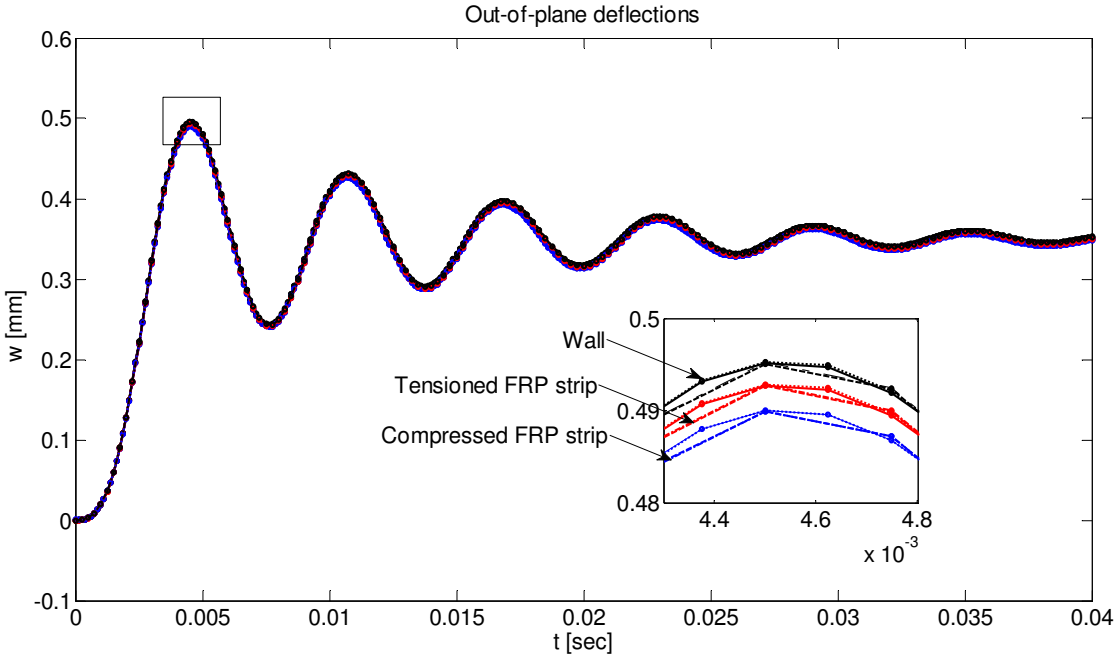

Figure 8. Out-of-plane deflections at mid-height versus time. Legend: – · – · – Mesh M2T1; – – – Mesh M3T1; · · · · · · Mesh M2T2; —— Mesh M3T2, ∘ time steps.

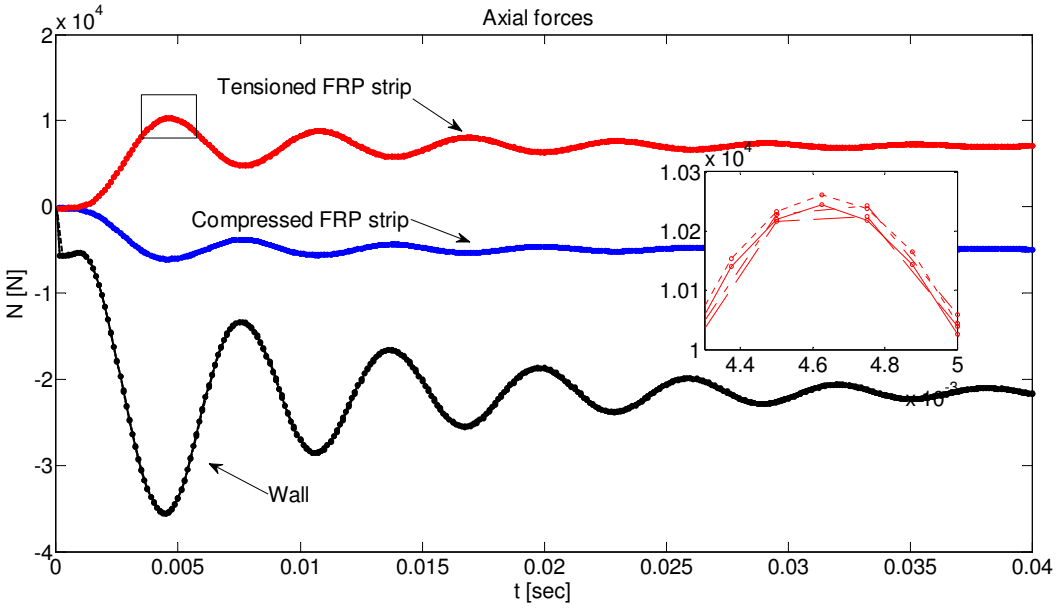

Figure 9. Axial forces at mid-height versus time. Legend: $-\cdot-\cdot-$ Mesh M2T1; $-\,-\,-$ Mesh M3T1; $\cdots\cdots$ Mesh M2T2; —— Mesh M3T2, $\circ$ time steps.

steady state solution. Due to the nonlinear-inelastic behavior and damage accumulation in the joints, the peak deflections at this case are slightly higher than in the case of static loading (Figure 3). A zoom plot on the first peak reveals the differences between the peak displacement of the masonry wall and those of the FRP strips. It also reveals that the differences between the various meshes are not significant and that a reasonable level of description can be achieved with a coarse mesh M2T1.

The time history of the axial forces in the wall and in the FRP strips at mid-height is studied in Figure 9. These results quantify the transient amplification of the forces due to the dynamic response and its rapid decay due to damping. It also reveals the evolution of a dynamic arching effect in which the global compressive force (the sum of axial forces in the wall and the FRP strips) is amplified due to cracking of the joint and the out-of-plane deflections, and varies in time. Also here, the effect of the arching force is more significant than the precompression. The zoom plot on the first peak in the response of the tensioned FRP strip reveals that the differences between the various meshes are not significant. In that sense, the relatively coarse mesh M2T1 provides an acceptable assessment of these aspects of the dynamic response.

The variation of the shear stresses in the adhesive layers is studied in Figure 10. The shear stresses are sampled near the middle joint at $x = 407.5$ mm (see Figure 6). In this location, both spatial meshes have nodes. The comparison between the results reveals some differences between the two spatial meshes. This is a result of the movement of the peak stresses with the refinement of the mesh. In the analysis with mesh M3, the peak stress travels from $x = 407.5$ mm to 408.75 mm, a node that does not exist in mesh M2. The zoom plot of the first temporary peak reveals that the differences between the analyses with the different time steps are rather minor and both of them provide an acceptable assessment of the nonlinear solution.

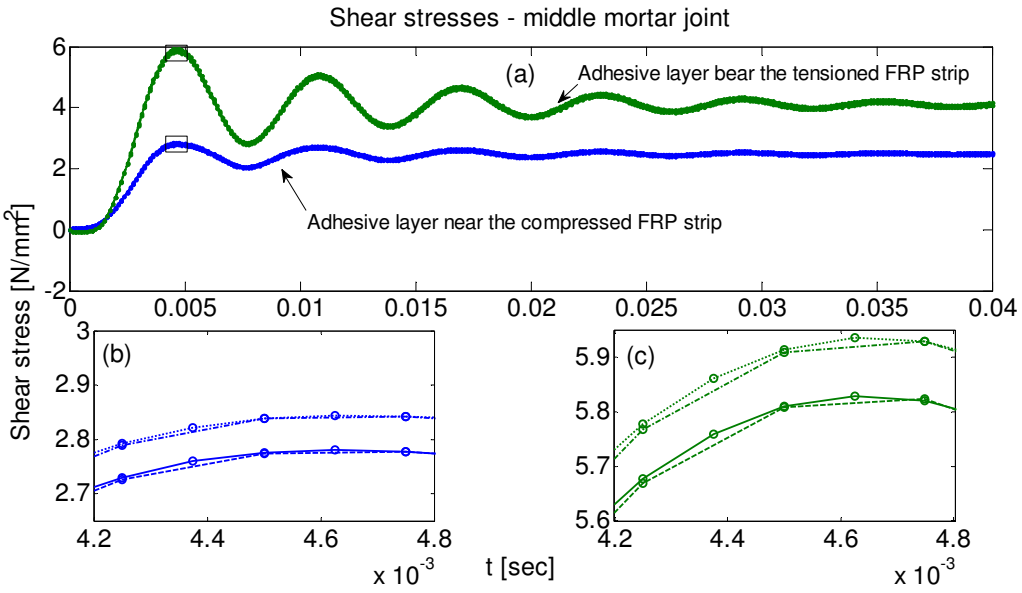

Figure 10. Peak shear stresses near the middle joint versus time. Legend: – · – · – Mesh M2T1; – – – Mesh M3T1; · · · · · · Mesh M2T2; —— Mesh M3T2, ∘ time steps.

The distributions of the dynamic axial forces (Figure 9) and the shear stresses (Figure 10) also clarify why in the static case the peak out-of-plane deflection of the compressed FRP strip is larger than that of tensioned strip (Figure 3, top half) whereas in the dynamic case it is the other way around (Figure 8). This shift is mainly attributed to the effect of the shear stresses near the joint and to the differences between the relative levels of axial tension/compression in the FRP strips. The interfacial shear stresses near the joints tend to increase the tensile force in the tensioned strip and to increase the compressive force in the compressed strip near the joint (see Figure 4, bottom half). The stresses are however, eccentric (with respect to the mid-surface of the FRP strips), evolve at the adhesive-FRP interface, and therefore yield localized bending in the FRP layer. This localized bending yields the slight "backwards deflection" (i.e., in the direction opposite to the global out-of-plane displacement), which can be observed in graphs (b) and (d) on the second row of Figure 3. Both in the static and in the dynamic cases studied here, the absolute value of the axial force in the tensioned FRP strip is larger than the one in the compressed strip and the magnitude of the shear stresses in the interface between adhesive and tensioned FRP interface are higher than in the interface between adhesive and compressed FRP strip (see Figure 6). Consequently, the effect of the backwards deflection in the tensioned FRP strip is larger than in the compressed one.

In the dynamic case, the ratio of the peak force in the tensioned strip over the peak one in the compressed strip (both in absolute values) and the ratio of the peak shear stress at the adhesive-tensioned strip interface over the peak one at the adhesive - compressed strip interface are slightly smaller than in the static case. As a result, in the dynamic case, the impact of the "backwards deflection" on the tensioned strip is slightly less prominent than in the static case and its effect on the compressed strip is slightly more prominent than in the static case. As the overall out-of-plane displacements combine the global ones with the localized bending effect near the joint, this yields the differences observed in the orders of the displacements in the static and the dynamic cases.

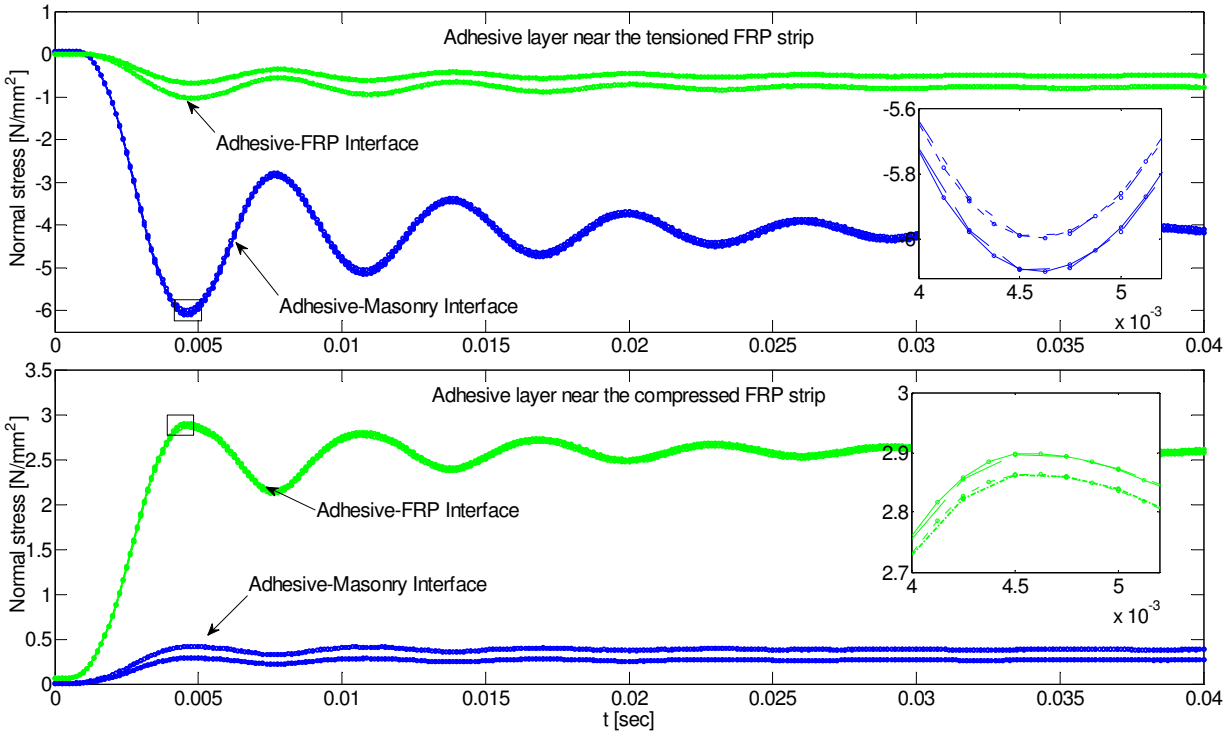

Figure 11. Out-of-plane normal stresses at $x = 415$ mm versus time. Legend: $-\cdot-\cdot-$ Mesh M2T1; $-\,-\,-$ Mesh M3T1; $\cdots\cdots$ Mesh M2T2; —— Mesh M3T2, ∘ time steps.

The evolution of the out-of-plane normal stresses at the interfaces of the inner and outer adhesive layers is studied in Figure 11. (The outer layer is the one that bonds the tensioned FRP strip.) The results are presented in terms of the stress at the middle of the specimen. The results capture and quantify the temporary amplification of the interfacial normal stresses, which are the main cause to premature debonding failures. In terms of numerical analysis, the curves reveal some differences between one spatial mesh and another. Yet, both analyses quantify a very similar pattern and the differences in terms of the peak values are not too significant. It is also observed that the differences between the temporal meshes are rather minor and they do not point at a prominent advantage of the refined mesh.

Finally, the analyses are compared in terms of run-time. The analysis with the coarse mesh M2T1 is considered as reference. The run-times of the analyses with meshes M2T2, M3T1, and M3T3 are 1.84, 2.64, and 4.51 times the reference run-time. This observation and the convergence characteristics discussed above indicate that mesh M2T1 may be sufficient for the dynamic analysis. Mesh M3T1 provides a good combination of accuracy and computation time.

4. Summary and conclusions

The dynamics of unidirectional FRP strengthened masonry walls has been investigated. In this part of the paper, a finite element for the nonlinear dynamic analysis of unidirectional strengthened masonry

walls has been developed. The finite element formulation has adopted a high-order theory approach in attempt to face the challenges associated with the combination of length scales, the significant differences in elastic properties, the presence of irregular points, the cracking and inelastic behavior of the mortar joints, and the layered structure of the strengthened wall. The finite element formulation has adopted a set of kinematic assumptions that stem form a high order representation of the static stress and displacement fields in the adhesive layer. This has allowed for the consideration of the variation of the stresses through the thickness of the adhesive layer and the evolution of interfacial stress concentrations while avoiding the divergence near irregular points and the increase in computational effort due to the 2D effects. The model has also taken into account the geometrical nonlinearity and has assumed that material nonlinearity due to cracking and crushing is concentrated in the mortar joints.

The performance of the analytical-numerical model has been examined through a static and dynamic convergence study. This study has pointed at the convergence characteristics of the model and has provided a measure of the level of refinement required in attempt to capture the localized effects. The numerical convergence study has indicated that the finite element model can overcome some of the critical problems encountered in standard FE analysis of strengthened walls. In that sense, it provided a computational framework that uses a 1D representation but can still handle the main features of the nonlinear dynamic response. The conversion of the above abilities into a FE based model allows for the use of standard computational and numerical procedures as well as for coupling with other elements and future implementation in a wider analysis framework.

References

[Albert et al. 2001] M. L. Albert, A. E. Elwi, and J. J. R. Cheng, "Strengthening of unreinforced masonry walls using FRPs", *J. Compos. Constr.* (*ASCE*) **5**:2 (2001), 76–84.

[Brush and Almroth 1975] D. O. Brush and B. O. Almroth, *Buckling of bars, plates, and shells*, McGraw-Hill, New York, 1975.

[Buller 2005] O. Buller, "Special finite element for the analysis of sandwich panels with a transversely flexible core", Master's thesis, Technion – Israel Institute of Technology, Haifa, 2005. In Hebrew.

[Clough and Penzien 1993] R. W. Clough and J. Penzien, *Dynamics of structures*, 2nd ed., McGraw-Hill, New York, 1993. Revised in 2010.

[Dafnis et al. 2002] A. Dafnis, H. Kolsch, and H.-G. Reimerdes, "Arching in masonry walls subjected to earthquake motions", *J. Struct. Eng.* (*ASCE*) **128**:2 (2002), 153–159.

[Davidson et al. 2005] J. S. Davidson, J. W. Fisher, M. I. Hammons, J. R. Porter, and R. J. Dinan, "Failure mechanisms of polymer-reinforced concrete masonry walls subjected to blast", *J. Struct. Eng.* (*ASCE*) **131**:8 (2005), 1194–1205.

[Dym and Shames 1973] C. L. Dym and I. H. Shames, *Solid mechanics: a variational approach*, McGraw-Hill, New York, 1973.

[Elmalich and Rabinovitch 2009] D. Elmalich and O. Rabinovitch, "Masonry and monolithic circular arches strengthened with composite materials: a finite element model", *Comput. Struct.* **87**:9–10 (2009), 521–533.

[Elmalich and Rabinovitch 2010] D. Elmalich and O. Rabinovitch, "Nonlinear analysis of masonry arches strengthened with composite materials", *J. Eng. Mech.* (*ASCE*) **136**:8 (2010), 996–1005.

[Fung 1965] Y. C. Fung, *Foundations of solid mechanics*, Prentice-Hall, Englewood Cliffs, NJ, 1965.

[Gao et al. 2006] B. Gao, J.-K. Kim, and C. K. Y. Leung, "Optimization of tapered end design for FRP strips bonded to RC beams", *Compos. Sci. Technol.* **66**:10 (2006), 1266–1273.

[Gilstrap and Dolan 1998] J. M. Gilstrap and C. W. Dolan, "Out-of-plane bending of FRP-reinforced masonry walls", *Compos. Sci. Technol.* **58**:8 (1998), 1277–1284.

[Griffith et al. 2004] M. C. Griffith, N. T. K. Lam, J. L. Wilson, and K. Doherty, "Experimental investigation of unreinforced brick masonry walls in flexure", *J. Struct. Eng.* (*ASCE*) **130**:3 (2004), 423–432.

[Hamed and Rabinovitch 2007a] E. Hamed and O. Rabinovitch, "Geometrically nonlinear effects in the flexural response of masonry walls strengthened with composite materials", *J. Mech. Mater. Struct.* **2**:5 (2007), 829–855.

[Hamed and Rabinovitch 2007b] E. Hamed and O. Rabinovitch, "Out-of-plane behavior of unreinforced masonry walls strengthened with FRP strips", *Compos. Sci. Technol.* **67**:3–4 (2007), 489–500.

[Hamed and Rabinovitch 2008] E. Hamed and O. Rabinovitch, "Masonry walls strengthened with composite materials: dynamic out-of-plane behavior", *Eur. J. Mech. A Solids* **27**:6 (2008), 1037–1059.

[Hamilton and Dolan 2001] H. R. Hamilton, III and C. W. Dolan, "Flexural capacity of glass FRP strengthened concrete masonry walls", *J. Compos. Constr.* (*ASCE*) **5**:3 (2001), 170–178.

[Huang and Lyons 2007] D. Huang and J. Lyons, "Numerical stress analysis of the bond between a reinforced concrete T-beam and FRP sheets", *J. Reinf. Plast. Compos.* **26**:12 (2007), 1225–1237.

[Khoshbakht et al. 2009] M. Khoshbakht, M. W. Lin, and C. A. Feickert, "A finite element model for hygrothermal analysis of masonry walls with FRP reinforcement", *Finite Elem. Anal. Des.* **45**:8–9 (2009), 511–518.

[Lam et al. 2003] N. T. K. Lam, M. Griffith, J. Wilson, and K. Doherty, "Time-history analysis of URM walls in out-of-plane flexure", *Eng. Struct.* **25**:6 (2003), 743–754.

[Li et al. 2009] L.-J. Li, Y.-C. Guo, P.-Y. Huang, F. Liu, J. Deng, and J. Zhu, "Interfacial stress analysis of RC beams strengthened with hybrid CFS and GFS", *Constr. Build. Mater.* **23**:6 (2009), 2394–2401.

[Newmark 1959] N. M. Newmark, "A method of computation of structural dynamics", *J. Eng. Mech. Div.* (*ASCE*) **85**:EM3 (1959), 67–94.

[Pan and Leung 2008] J. Pan and C. K. Y. Leung, "Effect of end tapering on crack-induced FRP debonding from the concrete substrate", *J. Compos. Constr.* (*ASCE*) **12**:1 (2008), 15–24.

[Rabinovitch 2004] O. Rabinovitch, "Nonlinear (buckling) effects in RC beams strengthened with composite materials subjected to compression", *Int. J. Solids Struct.* **41**:20 (2004), 5677–5695.

[Rabinovitch 2010] O. Rabinovitch, "Buckling-driven debonding in stiff block: compliant joint structural assemblies patched with composite materials", *Int. J. Fract.* **165**:1 (2010), 21–38.

[Rabinovitch and Frostig 2000] O. Rabinovitch and Y. Frostig, "Closed-form high-order analysis of RC beams strengthened with FRP strips", *J. Compos. Constr.* (*ASCE*) **4**:2 (2000), 65–74.

[Rabinovitch and Madah 2011] O. Rabinovitch and H. Madah, "Finite element modeling and shake-table testing of unidirectional infill masonry walls under out-of-plane dynamic loads", *Eng. Struct.* **33** (2011), 2683–2696.

[Rabinovitch and Madah 2012] O. Rabinovitch and H. Madah, "Dynamics of FRP strengthened unidirectional masonry walls, II: Experiments and comparison", *J. Mech. Mater. Struct.* **7** (2012), 29–44.

[Reddy 1999] J. N. Reddy, *Elastic plates*, Taylor & Francis, Philadelphia, 1999.

[Schwarts-Givli et al. 2007] H. Schwarts-Givli, O. Rabinovitch, and Y. Frostig, "High-order nonlinear contact effects in the dynamic behavior of delaminated sandwich panels with a flexible core", *Int. J. Solids Struct.* **44**:1 (2007), 77–99.

[Teng et al. 2002] J. G. Teng, J. W. Zhang, and S. T. Smith, "Interfacial stresses in reinforced concrete beams bonded with a soffit plate: a finite element study", *Constr. Build. Mater.* **16**:1 (2002), 1–14.

[Timoshenko and Gere 1961] S. P. Timoshenko and J. M. Gere, *Theory of elastic stability*, 2nd ed., McGraw-Hill, New York, 1961.

[Vinson and Sierakowski 1986] J. R. Vinson and R. L. Sierakowski, *The behavior of structures composed of composite materials*, Martinus-Nijhoff, Dordrecht, 1986. 2nd ed. published in 2002.

[Yang et al. 2004] Q. S. Yang, X. R. Peng, and A. K. H. Kwan, "Finite element analysis of interfacial stresses in FRP–RC hybrid beams", *Mech. Res. Commun.* **31**:3 (2004), 331–340.

Received 29 Aug 2010. Revised 9 Feb 2011. Accepted 10 Feb 2011.

ODED RABINOVITCH: cvoded@tx.technion.ac.il
Faculty of Civil and Environmental Engineering, Technion – Israel Institute of Technology, Haifa, 32000, Israel

HAZEM MADAH: hazem@tx.technion.ac.il
Faculty of Civil and Environmental Engineering, Technion – Israel Institute of Technology, Haifa, 32000, Israel

JOURNAL OF MECHANICS OF MATERIALS AND STRUCTURES

jomms.net

Founded by Charles R. Steele and Marie-Louise Steele

See http://jomms.net for submission guidelines.

JoMMS (ISSN 1559-3959) is published in 10 issues a year. The subscription price for 2012 is US $555/year for the electronic version, and $735/year (+$60 shipping outside the US) for print and electronic. Subscriptions, requests for back issues, and changes of address should be sent to Mathematical Sciences Publishers, Department of Mathematics, University of California, Berkeley, CA 94720–3840.

JoMMS peer-review and production is managed by EditFLOW® from Mathematical Sciences Publishers.

PUBLISHED BY
mathematical sciences publishers
http://msp.org/

A NON-PROFIT CORPORATION

Typeset in LaTeX

Journal of Mechanics of Materials and Structures

Volume 7, No. 1 January 2012

1559-3959(2012)7:1;1-D